Universidade de Aveiro **Departamento de física**
2012

Amanda Leigh Lorenz

N° 63689

Melhoramento de magnetos NdFeB pela via de recozimento com difusão

Improvement of NdFeB Permanent Magnets via Diffusion Annealing

Dissertação apresentada à Universidade de Aveiro para cumprimento dos requisitos necessários à obtenção do grau de Mestre em Ciência e Engenharia de Materiais/Functional Advanced Materials Engineering, realizada sob a orientação científica do Doutor Vitor Amaral, Professor Catedrático do Departamento de física da Universidade de Aveiro e do Doutor Manfred Rührig da Siemens AG.

European Commission
ERASMUS
MUNDUS

FAME MASTER

universidade de aveiro

Universität Augsburg

o júri

presidente

Prof. Dra. Florinda Costa
Professora Associada da Universidade de Aveiro

Prof. Dr. João Pedro Esteves de Araújo
Professor Auxiliar do Departamento de Física e Astronomia, Faculdade de Ciências, Universidade do Porto

Prof. Dr. Vítor Brás de Sequeira Amaral (orientador)
Professor catedrático da Universidade de Aveiro

Dr. Manfred Ruehrig (co-orientador)
Senior Research Scientist at Siemens AG, Erlangen, Germany

agradecimentos

I would to express my deep gratitude towards Prof. Dr. Vitor Amaral and Dr. Manfred Rührig for their guidance and support throughout the scope of this project.

Mr. Herbert Mai for all of his help during sample preparation and annealing.

I would like to thank Dr. Ferdinand Haider, Dr. Robert Horny, and Dr. Ana Barros for dedicating their time and effort in order to allow me the opportunity to participate in and complete my degree in the FAME network.

Additionally, I would like to thank the European Comission for supporting my studies.

Palavras chave

NdFeB, magnetos permanentes, disprósio, coercividade, recozimento difusão

Resumo

Os magnetos sinterizados de Nd-Fe-B, têm o maior produto de energia de todos os magnetos e têm vindo a substituir progressivamente os magnetos ferróicos em aplicações onde é necessária uma maior densidade de energia. São áreas como carros híbridos, acionamento de turbinas eólicas, bobines de motores, e também na miniaturização de dispositivos eletrónicos. Um parâmetro importante é a sua coercividade, e respetiva dependência na temperatura, que determina o intervalo de temperatura de aplicação. A fim de melhorar as temperaturas de funcionamento, elementos diversos, especialmente terras raras pesadas (HRE), tais como disprósio ou térbio, têm sido adicionadas como um meio de aumentar a coercividade, levando, no entanto, a uma diminuição da remanência. Embora as HREs sejam tradicionalmente incorporadas durante o processo de sinterização, foi demonstrado que a aplicação de uma camada superficial de Dy, seguida de recozimento pode exigir menos Dy, a fim de obter uma determinada coercividade. Este processo utiliza a difusão por fronteiras de grão (Grain Boundary Diffusion, GBD).

O objetivo deste trabalho foi reduzir a quantidade de Dy necessário para atingir um desejado aumento da coercividade em pequenos magnetos de Nd-Fe-B utilizando processos GBD e experimentação com adições de Cu. Os magnetos foram revestidos usando deposição física de vapor (PVD), sujeitos a tratamento térmico e, em seguida caracterizados utilizando técnicas de medição magnética, bem como microscopia electrónica de varrimento SEM. As medições magnéticas foram também usadas para avaliar o processo de difusão de Cu e Dy durante o recozimento. A coercividade aumentou com o tempo de recozimento, em que Dy é difundido no sistema, alcançando melhorias de cerca de 50% na coercividade. No entanto, a distância de difusão foi limitada a cerca de 100 µm a partir da superfície da amostra. Os aumentos relativos na coercitividade por unidade de Dy adicionado ao sistema usando GBD foram maiores do que com Dy incorporado durante a sinterização. A Inclusão de Cu não foi considerada benéfica para o sistema.

Keywords NdFeB, permanent magnets, dysprosium, coercivity, diffusion annealing

Abstract

Sintered Nd-Fe-B rare earth (RE) magnets have the highest energy product of any magnets and have been progressively replacing ferrous magnets in applications where a high energy density is needed. This pertains to areas such as hybrid cars, direct-drive wind turbines, voice coil motors, as well as the miniaturization of electronic devices. An important parameter of these magnets is their coercivity, respectively the temperature dependence thereof, which determines the temperature range accessible to the magnets. In order to improve the working temperatures, various elements, most notably heavy rare earth (HRE) elements such as dysprosium or terbium, have been alloyed in order to increase the coercivity; however, a remanence decrease results. Although HREs are traditionally included during the sintering process, it has been shown that applying the Dy as a coating after sintering followed by annealing may require less Dy in order to reach a given coercivity. This process is called Grain Boundary Diffusion (GBD).

The aim of this work was to reduce the amount of Dy needed to attain a desired increase in coercivity in small Nd-Fe-B magnets by employing GBD processes and experimentation with Cu additions. Magnets were coated using physical vapor deposition (PVD) techniques, heat treated, and then assessed using magnetic measurement techniques as well as scanning electron microscopy (SEM). Magnetic measurements were also used to assess the diffusion process of Dy and Cu into the magnets during annealing. The coercivity increased as annealing time progressed and Dy interdiffused throughout the system, reaching improvements in coercivity of about 50%. However, the diffusion distance was limited to about 100 µm from the sample surface. For small Dy additions, the relative gains in coercivity per unit Dy added to the system using GBD were greater than magnets with Dy incorporated during sintering. Inclusions of Cu were not found to be beneficial to the system.

Table of Contents

Table of Symbols

A	Exchange stiffness constant
A	Area
$\boldsymbol{B}$	Magnetic induction, flux density
$(BH)_{max}$	Maximum Energy Product
$B_J(y)$	Brillouin function
$\boldsymbol{B_r}$	Remanent magnetic flux
c	Concentration
C	Curie Constant
d	Grain size
D	Diffusivity
D_d	Dislocation diffusivity
D_{gb}	Grain boundary diffusivity
D^o_{gb}	Pre-exponential factor (Grain boundary diffusion)
D_s	Surface diffusivity
E_{ex}	Exchange energy
E_K	Magnetic anisotropy energy
E_{ms}	Magnetostrictive energy
E_W	Energy density of a Bloch Wall
g_J, g	Landé spectroscopic g-factor
H	Bulk enthalpy of diffusion
$\boldsymbol{H_{an}}$	Anisotropy field
$\boldsymbol{H}$	Magnetic field strength
$\boldsymbol{H_C}$	Coercive field
$\boldsymbol{H_{cB}}$	Inductive coercive field
$\boldsymbol{H_{cJ}}$	Polarization coercive field, intrinsic coercivity
$\boldsymbol{H_{cM}}$	Magnetization coercivity
$\boldsymbol{H_d}$	Demagnetizing field
H_{exch}	Heisenberg exchange energy
$\boldsymbol{H_{ext}}$	External magnetic field
H_{gb}	Grain boundary Enthalpy of Diffusion
ΔH_{gb}	Grain boundary activation enthalpy
$\boldsymbol{H_{int}}$	Internal magnetic field
$\boldsymbol{H_m}$	Exchange field, molecular field, Weiss field
$\boldsymbol{H_N}$	Nucleation field
$\boldsymbol{H_P}$	Pinning field
I	Current
$\boldsymbol{J}$	Total angular momentum
$\boldsymbol{J}$	Magnetic polarization
$J_{ij,\ aa,\ ab,\ bb}$, J_{exch}	Exchange coupling between nearest neighbor atoms
$\boldsymbol{J_r}$	Remanent magnetic polarization
$\boldsymbol{J_s}$	Saturation polarisation
k_B	Boltzmann constant
l	Orbital angular momentum quantum number
l	Diffusion length
$\boldsymbol{L}$	Total orbital angular momentum
l_{ex}	Exchange length
$K_{1,2}$	Magnetocrystalline anisotropy constant
$\boldsymbol{m_J}$, $\boldsymbol{m}$	Angular momentum quantum number
$\boldsymbol{m_l}$	Magnetic quantum number
$\boldsymbol{M_r}$	Remanent magnetization

$\boldsymbol{M_S}$	Saturation magnetization
$\boldsymbol{m_s}$	Spin quantum number
$\boldsymbol{M}$, $\boldsymbol{(M_{vol})}$	Magnetization (volume)
n	Principle quantum number
N	Number of atoms present in a system
N_d	Demagnetizing factor
n_{turn}	Windings per length of a solenoid
r_{ab}	Interatomic distance between atoms a, b
r_d	Radius of unfilled d-shell
R_{sd}	Critical radius for a single-domain particle
s	Segregation factor
S	Area under the $M(H)$ Hysteresis curve
$\boldsymbol{S_a}$, $\boldsymbol{S_b}$	Spin of atom a, b
$\boldsymbol{S}$, $\boldsymbol{S_{,ij}}$	Total angular spin momentum
SQ	Squareness coefficient
t	time
T	Temperature
T_c	Curie temperature
V	Volume
x	Position
δ	Grain boundary width
δ_W	Domain wall thickness
θ	Angle between spontaneous magnetization and the c-axis
θ_P	Paramagnetic ordering temperature
μ	Permeability
μ_B	Bohr magneton
$\boldsymbol{\mu_L}$	Magnetic moment due to orbital angular momentum
μ_o	Permeability of free space
$\boldsymbol{\mu_{obs}}$	Atomic magnetic moment
μ_r	Relative permeability
μ_{rev}	Reversible permeability
$\boldsymbol{\mu_S}$	Magnetic moment due to angular spin momentum
$\boldsymbol{\mu_{tot}}$	Total magnetic moment
ρ	Density
φ	Angle between spontaneous magnetization and the a-axis
ϕ	Magnetic flux through a magnet
χ	Volume susceptibility

Term	Symbol	SI Unit	cgs Unit
Magnetic Field Strength	$\boldsymbol{H}$	$10^3/4\pi$ A m^{-1}	=1 Oe
Volume Magnetization	$\boldsymbol{M}$	10^3 A m^{-1}	=1 Oe
Permeability	$\boldsymbol{\mu}$	10^{-3} J T^{-1}	=1 erg G^{-1}
Magnetic Flux Density, MagneticInduction	$\boldsymbol{B}$	10^{-4} T	=1 G
Susceptibility	$\boldsymbol{\chi}$	4π n.a.	=1 emu cm^{-3}
Magnetic Flux	$\boldsymbol{\phi}$	10^{-8} Wb, V s	=1 G cm^2
Magnetic Polarization	$\boldsymbol{J}$	10^{-4} T	=1 G
Demagnetization factor	$\boldsymbol{N_d}$	$1/4\pi$ n.a.	=1 n.a.

Table of Figures

Index of Tables

Chapter 1 - Background

1.1 Basic Properties of Magnetism

1.1.1 Molecular Foundations of Magnetism

Magnetism results from the orbital motion and spin angular momentum of electrons in a material. In order to understand the atomic origin of magnetism, there are several parameters that need to be defined. At the most basic level, there are four quantum numbers, determined using the Pauli Exclusion Principle and Hund's rules which specify the state of an electron:

1. *Principle quantum number,* n

The principle quantum number, n, determines the size of an electron's orbit and its energy. It can be any integer value higher than one, each integer referring to a distinct orbital arrangement. For example, electrons with values of n = 1, 2, 3… would occupy the K, L, M…-shells, respectively.

2. *Orbital angular momentum quantum number,* l

The orbital angular momentum quantum number l is determined by the shape of the electron orbital and can take values from 0 to (n - 1). Each integer value corresponds to a distinct orbital arrangement, for instance electrons with l = 1, 2, 3, 4… are referred to as s, p, d, f… electrons. l is used to determine the angular momentum of an electron due to its orbital motion and the possible values for the magnetic quantum number $\boldsymbol{m_l}$.

3. *Magnetic quantum number,* $\boldsymbol{m_l}$

The magnetic quantum number $\boldsymbol{m_l}$ characterizes the component of l in a specified ('quantized') direction, typically along that of the applied field. It can only take integer values from - l to l.

4. *Spin quantum number,* $\boldsymbol{m_s}$

The spin quantum number $\boldsymbol{m_s}$ is the angular momentum resulting from the rotation of the electron. The allowed values of $\boldsymbol{m_s}$ are ±½, depending on the electron spin direction/energy.

The four quantum numbers are used to determine the total angular momentum $\boldsymbol{L}$ and the total angular spin momentum $\boldsymbol{S}$. Together with the number of atoms present in a system N, $\boldsymbol{L}$ and $\boldsymbol{S}$ are used to characterize a magnetic system with localized moments.

The total angular spin momentum, $\boldsymbol{S}$, seen in Eq. (1), is the sum of the spin quantum numbers ($\boldsymbol{m_s}$) over all electrons bound to the atom. In short, $\boldsymbol{S}$ can be described as the [net number of 'up' spin electrons] x ½.

$$\boldsymbol{S} = \sum_i \boldsymbol{m}_{s_i} \tag{1}$$

The total orbital angular momentum $\boldsymbol{L}$ is the sum of all of the magnetic quantum numbers, as seen in Eq. (2).

$$\boldsymbol{L} = \sum_i \boldsymbol{m}_{l_i} \tag{2}$$

The resulting $\boldsymbol{L}$ and $\boldsymbol{S}$ are loosely coupled due to spin-orbit interaction, referred to as "Russell-Saunders Coupling". Spin-orbit interaction is responsible for orbital magnetism and the coupling of the spin system to the lattice. By combining the values for $\boldsymbol{L}$ and $\boldsymbol{S}$ in the ground state, the total angular momentum $\boldsymbol{J}$ can be calculated, again in conjunction with Hund's rules as follows:

- For less than ½ -filled shells: $\boldsymbol{J} = \boldsymbol{L} - \boldsymbol{S}$
  - The total 4f moments form parallel to 3d-element moments, i.e. light rare-earth elements
- For more than ½ -filled shells: $\boldsymbol{J} = \boldsymbol{L} + \boldsymbol{S}$
  - The total 4f moments form antiparallel to 3d moments, i.e. heavy rare-earth elements

This system can be applied to most magnetic materials. The magnetic properties of a system can be described once $\boldsymbol{S}$, $\boldsymbol{J}$ and $\boldsymbol{L}$ have been defined for an atom in the ground state and the number of atoms present in the system N is known. $\boldsymbol{J}$ is a vector quantity, and its value along a particular direction is described by the magnetic quantum number $\boldsymbol{m_l}$. The z-projection of the total angular momentum $\boldsymbol{J}$ is also called the secondary total angular momentum quantum number $\boldsymbol{m_J}$. The values of $\boldsymbol{m_J}$ range from $-\boldsymbol{J}$ to $\boldsymbol{J}$ in single integer steps.

The total magnetic moment is the sum of the moments due to $\boldsymbol{L}$ and $\boldsymbol{S}$ ($\boldsymbol{\mu_{tot}} = \boldsymbol{\mu_L} + \boldsymbol{\mu_S}$); however, due to interaction between $\boldsymbol{L}$ and $\boldsymbol{S}$ this is not the effective magnetic moment. The observed rare-earth magnetic moment ($\boldsymbol{\mu_{obs}}$), seen in Eq. (3), is the component of the total magnetic moment around $\boldsymbol{J}$ and determines the magnetic properties of the sample. In this equation, μ_B is the value of a Bohr magneton (μ_B = 9,274x10^{-24} Am², J/T). A Bohr magneton is the value of a fundamental quantum unit of the magnetic moment: each unpaired electron present in a system yields one Bohr magneton. g_J is the Landé spectroscopic g-factor, given in Eq. (4).

$$\boldsymbol{\mu}_{obs} = g_J \boldsymbol{J} \mu_B \tag{3}$$

$$g_J = 1 + \frac{\boldsymbol{J}(\boldsymbol{J}+1) + \boldsymbol{S}(\boldsymbol{S}+1) - \boldsymbol{L}(\boldsymbol{L}+1)}{2\boldsymbol{J}(\boldsymbol{J}+1)} \tag{4}$$

The magnetic moment as well as a plot of factors $\boldsymbol{L}$, $\boldsymbol{S}$, and $gJo + \sqrt{\boldsymbol{J}(\boldsymbol{J}+1)}$ for rare-earth elements are found in Figure 1.1.

The magnetization $\boldsymbol{M}$ is also a relatively simple calculation if the temperature of the material is at zero kelvin. In this case, only the lowest energy levels are occupied, so the total magnetization is simply the magnetic moment of a single atom multiplied by the number of atoms, N, in the system, as shown in Eq. (5)[1].

$$\boldsymbol{M}(T=0) = N g_J \boldsymbol{m}_J \mu_B = N g_J \mu_B \boldsymbol{J} \tag{5}$$

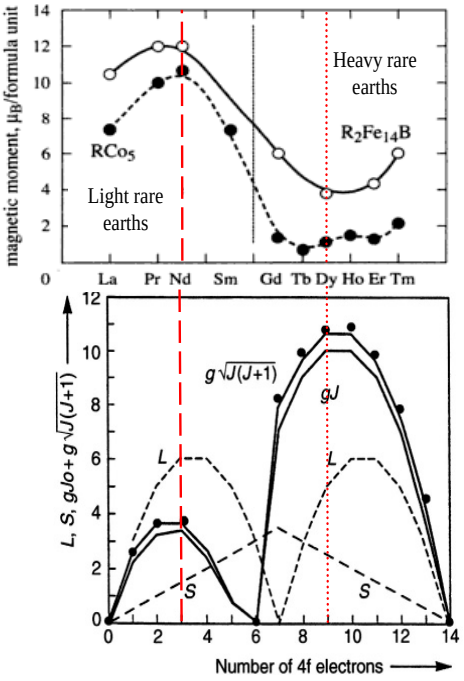

Figure 1.1. Comparison of the magnetic moment in RCo_5 and $R_2Fe_{14}B$ compounds[1] and factors $\boldsymbol{L}$, $\boldsymbol{S}$, and $gJo + \sqrt{J(J+1)}$ [2] for the rare earth elements.

Several models are available in order to determine the spontaneous magnetization in a solid, including the mean-field Ising model and the Heisenberg Hamiltonian; however, the details of these models will not be discussed here. At non-zero temperatures, the possibility of electrons being excited to higher levels exists and statistical calculations must be considered; the Boltzmann distribution is then employed and calculations of magnetization at non-zero temperatures (Eq. (6)) contain the so-called 'Brillouin function' $B_J(y)$. The form of this function for individual materials has an important effect on the behavior at non-zero temperatures. The Brillouin function describes the dependence of the magnetization on the total angular momentum $\boldsymbol{J}$, the g-factor g_J, the temperature T, and the applied field $\boldsymbol{H}$ responsible for $(2\boldsymbol{J}+1)$ splitting of levels which are degenerate in the absence of a field.

[1] This is the same as the saturation magnetization in ferromagnetic materials.

$$M(T) = Ng_J \mu_B \boldsymbol{J} B_J(y)$$
$$y = \frac{g_J \mu_B \boldsymbol{J} \mu_o \boldsymbol{H}}{k_B T} \quad (6)$$

Another way of viewing magnetism in a material containing independent, non-interacting ions is the sum of the magnetic moments. If this is divided by the volume of the sample, the volume magnetization, which is a material property, may be calculated as in Eq. (7).

$$\boldsymbol{M}_{vol} = \frac{1}{V}\sum \boldsymbol{\mu} \quad (7)$$

1.1.2 Magnetic Field, Magnetization, Polarization, Induction

Three properties which are essential when discussing magnetic materials are the magnetic field strength $\boldsymbol{H}$ [A m^{-1}, Oe], the induction $\boldsymbol{B}$ [T, G] and the magnetization $\boldsymbol{M}$ [A m^{-1}, Oe]. Each of these are vector quantities, the relative directions of which are given in Figure 1.2.

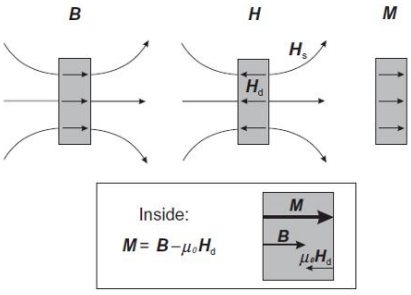

Figure 1.2. Illustration of the directions B, H, and M.[3]

The field strength $\boldsymbol{H}$, also called the magnetizing force, describes some force working to bring the magnetic moments of a material into alignment. The internal magnetic field $\boldsymbol{H_{int}}$ is dependent on the external field applied to the sample $\boldsymbol{H_{ext}}$, as well as the demagnetizing field $\boldsymbol{H_d}$ within a sample. The demagnetizing field is given by the magnetization $\boldsymbol{M}$ scaled by the demagnetizing factor N_d. N_d is a dimensionless number between zero and one and is dependent on the shape of the magnet. Equations (8) and (9) show how the internal and demagnetization fields are determined. The reaction of a magnetic moment with an externally applied field results in Zeeman splitting, which leads to the alignment of moments in magnetic materials.

$$\boldsymbol{H}_{\text{int}} = \boldsymbol{H}_{ext} + \boldsymbol{H}_d \quad (8)$$

$$\boldsymbol{H}_d = -N_d \boldsymbol{M} \quad (9)$$

The magnetization $\boldsymbol{M}$ of a sample is the density of magnetic moments and depends on $\boldsymbol{H}$, as described in Eq. (6). Often, the magnetic polarization $\boldsymbol{J}$ [T] is used instead of the magnetization. The two may be equated using Eq. (10).

$$\boldsymbol{J} = \mu_o \boldsymbol{M} \tag{10}$$

The magnetic induction $\boldsymbol{B}$, also called magnetic flux density, describes the magnetic field inside a material. Magnetic induction is caused by both external and Amperian (atomic) currents. The most general equation for internal induction $\boldsymbol{B_{int}}$ is presented in Eq. (11). Because of the potential influence of external factors, $\boldsymbol{M}$ may be considered a preferred means of characterizing magnetic materials. In para and diamagnetic materials internal induction $\boldsymbol{B_{int}}$ is related to the external field $\boldsymbol{H_{ext}}$ and $\boldsymbol{M}$ by the vacuum permeability, as in Eq. (12)[2]. This assumes that there are no demagnetizing fields in the material. $\boldsymbol{B}$ may also be redefined in terms of the susceptibility χ and permeability μ. In free space, $\boldsymbol{B}$ and $\boldsymbol{H}$ are equal (the susceptibility is zero), but when a material is involved, $\boldsymbol{M}$ must also be included.

$$\boldsymbol{B_{int}} = \mu_o(\boldsymbol{H_{int}} + \boldsymbol{M}) \tag{11}$$

$$\boldsymbol{B_{int}} = \mu_o \cdot \mu_r(\boldsymbol{H_{ext}}) \cdot \boldsymbol{H_{ext}} = \mu_o(\boldsymbol{H_{ext}} + \boldsymbol{M}) \tag{12}$$

In the latter of the above equations, μ_r is the relative permeability ($\mu_r = \mu/\mu_o$), a dimensionless number. In ferro- and ferrimagnetic materials, the relation between $\boldsymbol{B}$ and $\boldsymbol{H}$ becomes non-linear, resulting in a slope in the hysteresis loop where $\mu_r >> 1$. Eq. (12) is not valid for approximating the internal field of ferromagnetic materials because it neglects the intrinsic demagnetizing field $\boldsymbol{H_d}$ inside the sample. Eq. (13) presents $\boldsymbol{B_{int}}$ for ferromagnetic materials in absence of an applied field.

$$\boldsymbol{B_{int}} = \mu_o(\boldsymbol{M} + \boldsymbol{H_d}) = \mu_o \boldsymbol{M}(1 - \boldsymbol{N_d}) = \boldsymbol{J} + \mu_o \boldsymbol{H}_d \tag{13}$$

1.1.3 Exchange Interaction Energy

The exchange interaction energy, also called the Heisenberg exchange energy H_{exch}, is used to describe orientation of electrons spins and magnetic moments in adjacent atoms, for instance if they are oriented parallel or antiparallel to one-another. It is the largest of the magnetic interactions and can be given by the Heisenberg Hamiltonian, Eq. (14) , in which J_{ij} (also denoted J_{exch}) is the exchange integral[3] and $\boldsymbol{S_{i,j}}$ is the spin of a given atom. The summation includes all spin pairs in the crystal lattice. However, in most cases it suffices to consider only the spins of neighboring atoms. The Heisenberg model is used to describe the quantum-mechanical exchange interaction between atomic spins in systems with localized magnetic moments.

[2] Para-and diamagnetic materials

[3] The exchange integral is a quantity, related to the distance between the atoms considered amongst other things. It is a measure of the interatomic magnetic order.

$$H_{exch} = -2\sum_{i<j}^{N} J_{ij}\boldsymbol{S}_i \cdot \boldsymbol{S}_j \qquad (14)$$

(Heisenberg Hamiltonian[3])

Many magnetic compounds (especially antiferro- and ferrimagnetic materials) can be described as containing two (or more) interpenetrating sublattices, hereby denoted A and B. The atoms in each of these sublattices exist in unique crystallographic environments. J_{ab} characterizes the exchange coupling between two nearest-neighbor spins present on different sublattices, while J_{aa} and J_{bb} would denote those on the same sublattice. The exchange interaction gives rise to an effective internal field called the *exchange field, molecular field,* or *Weiss field,* $\boldsymbol{H_m}$; this field exists even in the absence of an external field.

The exchange integral between sublattices is used to determine if a material is ferromagnetic, antiferromagnetic, or ferrimagnetic, as shown below. If $J_{ab} > 0$, the wave functions are non-symmetric and the electron spins are oriented parallel to one-another: a ferromagnetic interaction occurs. Likewise, if $J_{ab} < 0$, the electron spins are oriented antiparallel to one another, the wave functions are symmetric and electrons experience an antiferromagnetic interaction (Figure 1.3).

Ferromagnetic	$\boldsymbol{J_{aa} > 0}$
Antiferromagnetic	$\boldsymbol{J_{ab} < 0,\quad J_{aa} = J_{bb}}$
Ferrimagnetic	$\boldsymbol{J_{ab} < 0,\quad J_{aa} \neq J_{bb}}$

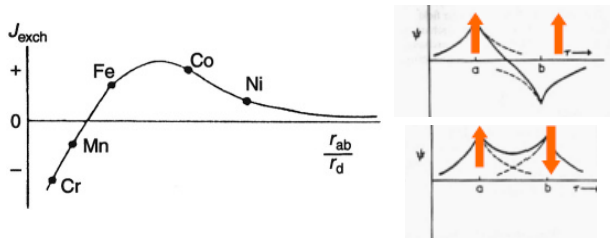

Figure 1.3. The Bethe-Slater curve[2], describing the relationship between the J_{exch} and r_{ab}/r_d with the corresponding wave functions and spin orientations.[4]

One of the important consequences of the exchange interaction is that the distance between two atoms can result in the spins of those being parallel or antiparallel to one another. When considering adjacent atoms, the interaction is said to be a 'direct exchange' interaction, which is pertinent to 3d elements. The nature of the exchange interaction is also dependent on the ratio of the interatomic distances and the radius of the

incompletely-filled d-shell, r_{ab}/r_d. A large ratio is correlated to a positive exchange constant, while a small value is indicative of a negative exchange constant.

At more medial values (between Fe and Co) the exchange constant reaches a maximum, as seen in Figure 1.3, also known as the Bethe-Slater curve. This curve is generally used to describe the magnetic moment coupling, although it may not be applicable to all situations as it lacks sound theoretical basis. The positive exchange interaction between neighboring magnetic moments is the reason for the ferromagnetic state of Fe, Co and Ni.

1.1.4 Curie Temperature

As the temperature increases, the alignment of the magnetic moments may become unstable, and at a certain point the competition between interatomic exchange and thermal disorder leads to the disruption of spontaneous polarization. The temperature at which ferromagnetic materials become paramagnetic is defined as the Curie temperature, T_c. At T_c, the spontaneous magnetization declines or vanishes not because of a reduction of the magnitude of the magnetic moments, but rather a rotation of moments to a disordered state. The Curie law[4] and a variation thereof (the Curie Weiss law, in which the paramagnetic Curie temperature θ_P is also included) are used to describe the susceptibility of magnetic materials above critical temperatures. The Curie-Weiss Law is shown below in Eq. (15), in which θ_P may be substituted by the Curie temperature T_C in ferromagnetic materials and C is the Curie constant, as defined in Eq.(16). The reciprocal of the susceptibility when plotted against the temperature is a linear function, the intercept of which is θ_P.

$$\chi = \frac{C}{T - \theta_p} \tag{15}$$

(Curie-Weiss Law)

$$C = \frac{N\mu_o g^2 J(J+1)\mu_B^2}{3k_B} \tag{16}$$

The Curie temperature has important implications on the feasible working temperatures of magnets. At temperatures above T_c, generated hysteresis loops become closed and less square-like. Below the Curie temperature, it can be shown that the decrease in magnetization with temperature is dependent only on the form of the Brillouin function (See 1.1.1 Molecular Foundations of Magnetism), and is independent of material

[4] The Curie Law is used to describe Langevin paramagnetism

parameters such as the atomic number, number of magnetic atoms being considered, or the value of T_C.

1.1.5 Magnetic Anisotropy

Magnetic anisotropy refers to the tendency or ability of the magnetic moments in a material to remain oriented in a preferred direction, due to a minimized energy. The anisotropy energy explains the existence of 'easy' and 'hard' directions of magnetization within a magnet. When oriented along 'easy directions', atomic moments have a lower energy compared to those along other directions. Accordingly, when fields are applied along the easy direction, materials are more susceptible and the saturation magnetization is reached at lower applied fields (see Figure 1.4). Hard magnets are characterized by a strong preference to be aligned along the easy axis. Magnetic anisotropy may be categorized in several manners:

- *Magnetocrystalline anisotropy* due to the atomic structure of the material
- *Shape anisotropy* due to the shape of the bulk magnet
- *Induced magnetic anisotropy* due to tempering the sample in an applied field
- *Stress anisotropy* due to magnetostriction[5]
- *Surface and interface anisotropy*

Magnetocrystalline anisotropy is one of the most important factors for the rare earth (RE) based permanent magnets investigated in this work. Other types of permanent magnets (i.e. AlNiCo) rely on shape anisotropy caused by their microstructure.

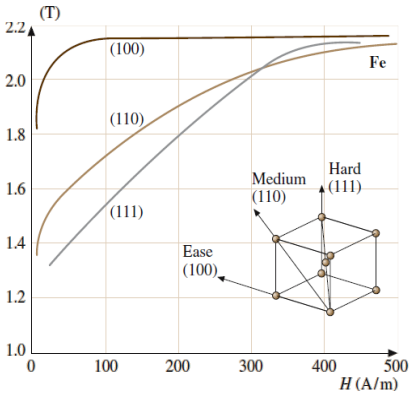

Figure 1.4. Magnetization curves for Fe single crystal in several directions as an indication of magnetocrystalline anisotropy.[5]

Magnetocrystalline anisotropy results from spin-orbit interaction[6] of the inner d-electrons (in Fe, Ni, and Co) and f-electrons (in rare-earth elements). Magnetic moments in a material will have some preferred direction because the atomic wave functions of the d- and f-orbitals are non-spherical, leading to nondegenerate spatial orientations. The anisotropy displayed by the RE

[5] Magnetostriction is spontaneous deformation that occurs during magnetization. Because the crystal lattice is coupled to the orbital, and the orbital to the electron spin, when the spin changes direction, the lattice inside a magnetic domain is deformed. Despite a change in shape, the volume must remain constant, resulting in induced stresses scaling with the applied field until it reaches a saturation point.

[6] This interaction causes a crystal field

sublattice in RE permanent magnets is responsible for the anisotropic properties of such materials. If moments are to be aligned along the hard direction of a material, the Zeeman interaction must overcome the spin-orbit coupling[7].

The magnetocrystalline anisotropy energies K_1, K_2, etc. characterize the anisotropic properties of materials and allow one to calculate the anisotropy energy dependence, as in Eq. (17) (for tetragonal systems). In this equation, θ and φ give the polar angles between the spontaneous magnetization and the c-axis or a-axis, respectively (see Figure 1.5). When aligned in the direction of easy magnetization, $K = 0$. Typically evaluating only K_1 and K_2 is considered sufficient.

$$E_K(\theta,\varphi) = K_1 \sin^2\theta + K_2 \sin^4\theta + K_3 \sin^4\theta \cos 4\varphi \qquad (17)$$

K_1 (uniaxial term) gives insight into the preferred orientation of the magnetic moment with respect to the c-axis. If K_1 is the dominant term[8], two possible cases result:

1. $K_1 > 0$ (i.e. Ce, Pr, Nd, Tb, Dy, Ho) - the magnetic moment is parallel to the c-axis.
2. $K_1 < 0$ (i.e. Sm, Er, Tm, Yb) - the magnetic moment is perpendicular to the c-axis.

Only the elements of the first case are considered practical for use in $R_2Fe_{14}B$ magnets because preferred direction of the latter may lie anywhere in the xy-basal plane rather than along a well-defined axis. Through considering the magnetic coupling in such magnets, it could also be shown that for *R = Ce, Pr*, and *Nd* the magnetic moments are parallel to Fe. On the contrary, for *R = Tb, Dy*, and *Ho* the moments are coupled antiparallel to Fe, thus reducing the saturation magnetization.

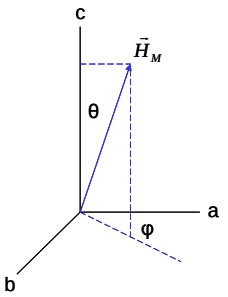

Figure 1.5. Moment direction relative to c-axis.

The anisotropy of a magnetic material can be qualitatively described by comparing the directions of hard and easy magnetization. The anisotropy field within a material $\boldsymbol{H_{an}}$ is obtained by measuring the sample at directions parallel and perpendicular to the axis of easy magnetization and is used to estimate the anisotropy constants. In many cases, the anisotropy field can be estimated by Eq. (18), in which $\boldsymbol{J_s}$ is the saturation polarization. This describes, in theory, the internal anisotropy field and

[7] The Zeeman interaction describes the interaction of the crystal with an external field causing splitting, whereas the spin-orbit coupling maintains the preferred orientation of magnetic moments and can be viewed as a kind of restoring torque.

[8] Other directions will be more relevant if K_1 is not the dominating factor; these are not suitable for magnetic applications as there is no anisotropy-energy barrier preventing them from realigning in an opposite direction (any position perpendicular to the c-axis may be chosen).

hence the theoretical magnitude of the counter-acting field necessary in order to demagnetize the sample. However, domain reversal often begins at field strengths much lower than this due to the generation of reverse domains and Bloch walls.

$$\boldsymbol{H_{an}} = {}^{2K_1}\!\!\diagup\!\!_{J_S} \tag{18}$$

1.1.6 Magnetic Domains and Bloch Walls

Magnetic domains are areas in which the magnetic moments are aligned along a coherent axis. In non-magnetized samples domains still exist; however, they are small and randomly oriented, yielding zero net magnetization. One microstructural grain may encompass many magnetic domains. The total flux out of any closed surface must be zero (given by Gauss' law of magnetism). This implies that the flux lines of a magnetic field form closed loops. Magnetic materials with few domains have what is called stray field, which is the extension of magnetic field lines to an area outside of the material. This leads to an increase in the magnetostatic energy of the system, and is unfavorable. In order to minimize the energy, a magnetic material will sporadically separate into several domains in order to reduce the stray field, resulting in a domain structure (see Figure 1.6). The ideal domain structure has the domains oriented at 90° angles to one-another, thus forming closed loops within the material (no stray field). The final structure is determined by balancing the reduction of stray field with the energy increase from orienting some spins away from the easy axis.

If an external field of sufficient magnitude is applied, domains oriented in the direction of the field will grow at the expense of improperly-oriented domains. An energy balance must be reached before the final magnetic microstructure is achieved. This includes the exchange energy needed to change the direction of a spin E_{ex}, the magnetostrictive energy from stresses induced via small changes to the shape of the crystal lattice E_{ms}, and the anisotropy energy E_K.

Bloch walls are boundaries between magnetic domains, in which the alignment of magnetic spins are gradually reoriented before reaching the next magnetic domain. Figure 1.6 shows the variation in E_{ex} and E_K across a Bloch wall. Whether the magnetic domains are being reoriented sporadically or with the aid of an external field, the creation and movement of the Bloch walls requires energy. Hence, in order to rearrange the magnetic domains, the energy reduction experienced by the system must outweigh the cost needed

to reorient magnetic spins and move Bloch walls. The realignment of magnetic domains is what is qualitatively seen in the hysteresis loop (See Figure 1.7 and Figure 1.8).

Magnetic anisotropy again becomes an important factor in the domain structure, as domains with lower anisotropy may be broken-up more easily. The bulk domain wall thickness δ_W is a result of competition between the anisotropy constant K_1 and the magnetic exchange stiffness A (the chance of having parallel spins) as in Eq. (19)[8].

$$\delta_W \propto \sqrt{\frac{A}{K_1}} \tag{19}$$

The widths of domain walls typically vary from several lattice spacings (a few nm), up to about 100 nm, so the turning of magnetic moments is very gradual due to exchange coupling (making abrupt direction changes unfavorable). However, there is a competition with E_K which favors collinear spins along the axis of easy magnetization and so increasing E_K tends to decrease the width of the domain wall due to the deviation of the magnetic moments away from this axis.

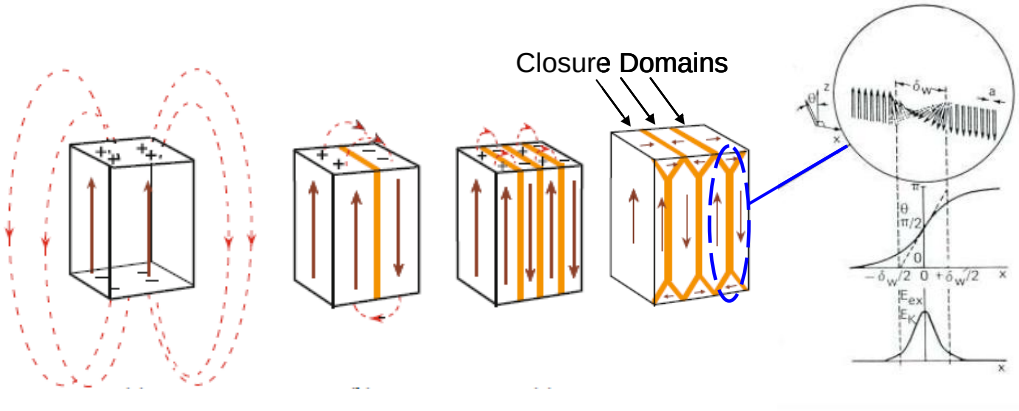

Figure 1.6. Development of closure domains and a schematic of a Bloch wall transition with corresponding relative values of the E_{ex} and E_k. Adapted from [6] and [7].

Bloch walls will only form if the gain in magnetostatic energy is greater than the Bloch wall energy. The Bloch wall width in materials can, generally speaking, be reduced by refining the grain size within magnetic materials. If the size of the grain is reduced to the point that it can only encompass one magnetic domain, the Bloch wall size may be reduced to insignificant dimensions or be eliminated[9]. Eq. (20)[8] gives the energy density of a Bloch

[9] This gives rise to phenomena such as superparamagnetism, in which the magnetic moments in a material all change direction at the same time rather than gradually.

wall E_W. Table 1.1 shows some values related to the formation of magnetic domains and Bloch walls.

$$E_W \propto \sqrt{AK_1} \tag{20}$$

Table 1.1. Micromagnetic parameters at room temperature.[8]

Property	Fe	$SmCo_5$	$Nd_2Fe_{14}B$
A (pJ/m)	8,3	22	7,7
K_1 (MJ/m³)	0,05	17	4,9
δ_W (nm)	40,0	3,6	3,9
E_w (mJ/m²)	2,6	77	25
l_{ex} (nm)	1,5	4,9	1,9
R_{sd} (nm)	6	764	107

*R_{sd} is the critical radius for a single domain, the radius for which domain formation is favorable

1.1.6.1 Bloch Walls and Nucleation Mechanisms

The nucleation of Bloch walls and growth of reverse domains is the reason that demagnetization is able to occur at much lower fields ($\boldsymbol{H_c < H_{an}}$) than those predicted theoretically using parameters such as Eq. (18). This is because the movement of a Bloch wall requires less energy than a simultaneous flip of the entire system orientation, as this only affects the area around the wall surface rather than the entire material volume. Bloch walls may nucleate more easily at defect regions (i.e. grain boundaries, defects, etc.): these are areas in which the exchange field and anisotropy field have been reduced in comparison to the bulk. Demagnetization via Bloch wall growth is dominant in materials having high magnetocrystalline anisotropy.

Although defects may serve as nucleation points for reverse domains, they may also work to impede the growth of magnetic domains. There are two general mechanisms used to describe the movement of Bloch walls throughout a magnetic system: *nucleation*-controlled and *pinning*-controlled, which largely dependent on the nucleation field $\boldsymbol{H_N}$ or pinning field $\boldsymbol{H_P}$, respectively. Both $\boldsymbol{H_N}$ and $\boldsymbol{H_P}$ are directly related to the material anisotropy. A schematic of the virgin curves of the hysteresis loop for each mechanism is given in Figure 1.7.

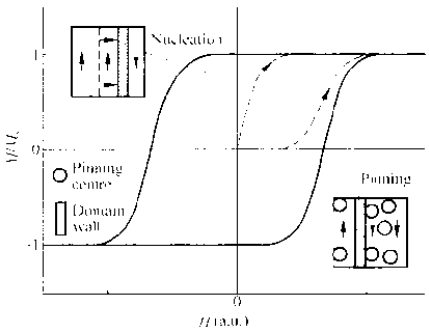

Figure 1.7. Virgin curves for pinning- and nucleation-controlled materials.[8]

In *nucleation-type* magnets, the motion of Bloch walls through magnetic grains is relatively easy, and pinning occurs primarily at grain boundaries. However, once the magnet is fully

saturated, it is very difficult to generate (nucleate) reverse domains. Thus the coercivity is determined by the nucleation field of reverse domains. Optimal grain structure, smooth grain boundaries and high anisotropies at grain boundaries together with a small number of defects are prerequisites for good nucleation-type magnets.

The origin of reverse domains is widely accepted to be localized regions of reduced anisotropy, which may include interfaces between the main phase and Nd-rich phases[9],surfaces which may be damaged due to machining[10, 11], magnetically-coupled grains, misaligned grains, magnetically perturbed grain surfaces, defects[12] and sharp corners at the grain edges that which may cause large local demagnetizing fields[13]. In theory, once a reverse magnetic domain forms at one of these points, it is believed to then propagate throughout the grains and the bulk structure relatively easily.

A different mechanism exists in *pinning-type* magnets. Here, reverse domain nucleation is fairly easy, but the movement of the domain walls within the grains is strongly hindered by pinning sites (i.e. inhomogeneities in the size of Bloch wall width). Unless the field is sufficiently strong, the wall is able to bend but not move forward. In pinning-type permanent magnets the pinning strength determines the coercivity.

The difference between nucleation and pinning type permanent magnets can be best distinguished by the virgin curve of the hysteresis loop. Materials such as $SmCo_7$ are pinning controlled. If the field required to free a boundary from pinning $\boldsymbol{H_P}$ is larger than that for nucleation $\boldsymbol{H_N}$, then $\boldsymbol{H_C} = \boldsymbol{H_P}$ and domain growth follows what is called 'inhomogeneous pinning-controlled coercivity'. However, as long as the applied field remains lower than $\boldsymbol{H_P}$, existing reverse domains will remain pinned at the grain boundaries and the hysteresis curve looks very similar to that where $\boldsymbol{H_P} < \boldsymbol{H_N}$. Examples of nucleation-controlled magnets include $SmCo_5$ and $Nd_2Fe_{14}B$.

1.1.7 Rare-earth and 3d Metal Alloys

Magnets employed in high-performance applications are typically composed of some mixture of rare-earth and 3d-metal elements, each of these composing their own sublattice. The rare-earth sublattice provides high magnetocrystalline anisotropy, high magnetostriction and high magnetic moments; the 3d sublattice causes a high magnetic ordering temperature. The two sublattices must be strongly coupled in order to obtain optimal magnetic properties.

The total 4f moment for heavy rare earth metals ($\boldsymbol{J} = \boldsymbol{L} + \boldsymbol{S}$) is coupled antiparallel to the 3d moment, and the total 4f moment for heavy rare earth metals ($\boldsymbol{J} = \boldsymbol{L} - \boldsymbol{S}$) is coupled

parallel to the 3d moment. The calculation of the total angular momentum makes this clear (*1.1.1 Molecular Foundations of Magnetism*). The reader is also directed to section *1.1.5 Magnetic* Anisotropy as well as section *1.3 NdFeB Magnets* for further insight into these materials.

1.1.8 Permanent Magnet Characterization and Hysteresis Loops

Recording the hysteresis loop i.e. $\boldsymbol{J(H)}$ or $\boldsymbol{B(H)}$ is the most recognizable tool to characterize the extrinsic properties of ferromagnetic materials. From the hysteresis loop several material parameters can be extracted: the most important of which for practical uses are the coercive field $\boldsymbol{H_c}$, the remanent magnetization $\boldsymbol{B_r}$, the saturation magnetization $\boldsymbol{M_s}$ and the maximum energy product $(BH)_{max}$. An example of such a plot is found in Figure 1.8. A hysteresis plot is generated by measuring the flux density $\boldsymbol{B}$ inside a magnet after exposing the sample to an external field $\boldsymbol{H}$ which is large enough to (re)align all of the magnetic domains within the sample. Additionally, the polarization $\boldsymbol{J}$ of the sample may be calculated as a function of the magnetization (Eq. (10)). The area covered (enclosed) by the hysteresis loop expresses an energy density [T*A/m = Ws/m³ = J/m³] and corresponds to the remagnetization losses for a full re-magnetization cycle. Soft magnetic materials display narrow hysteresis curves (small magnetization losses, i.e weak resistance against re-magnetization) while hard magnetic materials display broader, more square-like $\boldsymbol{J(H)}$ or $\boldsymbol{M(H)}$ loops (high magnetization losses, i.e. higher resistance against re-magnetization).

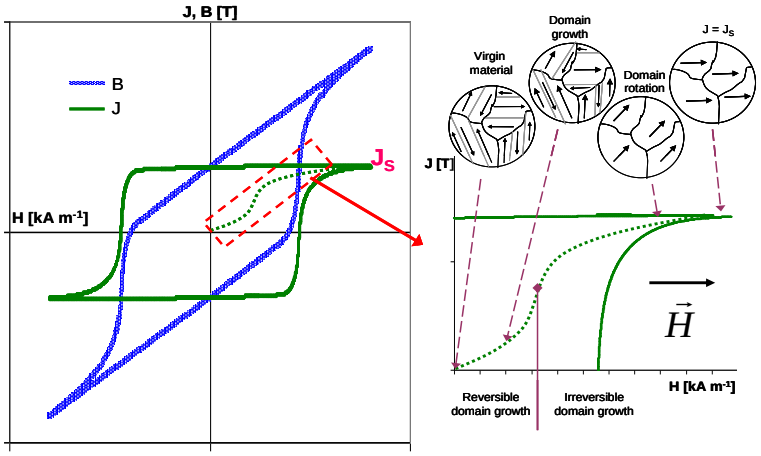

Figure 1.8. Full hysteresis curve and schematic of domain configurations along the virgin curve, adapted from [14].

During initial magnetization of the sample, the 'virgin curve' is created, starting in the demagnetized state ($\boldsymbol{J} = 0$). When increasing the external field, domains aligned along the field direction grow on the expense of domains with opposite direction. Initially, domain growth is reversible; however, as domains are able to move past defects and pinning

locations, a region of irreversible growth is reached. As soon as the increase in a magnetization component along the field direction by domain wall movement ceases, the magnetization can only further align along the field direction by domain rotation processes A schematic of this is shown in Figure 1.8. At $\boldsymbol{M_s}$, all magnetic domains are aligned.

Following initial magnetization, an external field which is opposite to the magnetization direction of the sample is applied and the internal field is again measured. This results in reversal of the sample magnetization. By varying the intensity of the applied field, a hysteresis curve may be generated, and $\boldsymbol{H_c}$, and $\boldsymbol{B_r}$ may be measured. $\boldsymbol{H}$ is measured by using a test coil and Ampere's law, and the $\boldsymbol{B}$ is defined by the magnetic flux over a permeated area, as seen in Eqs. (21) and (22), respectively. The polarization can then be calculated from the measured $\boldsymbol{B}$ and $\boldsymbol{H}$ by combining Eqs. (10) and (11), and removing the effect of the applied field on the measurement (Eq. (23)).

$$\boldsymbol{H} = I \cdot n_{turn} = \frac{current[A] \cdot \#turns}{length[m]} \tag{21}$$

$$\boldsymbol{B} = \frac{\Delta\varphi}{\Delta A} = \frac{Magnetic\ flux\ [Vs]}{Permeated\ area\ [m^2]} \tag{22}$$

$$\boldsymbol{J} = \boldsymbol{B} - \mu_o \boldsymbol{H} = \mu_o \boldsymbol{M} \tag{23}$$

The second quadrant is the most important when determining the practical uses of permanent magnets. The coercivity of magnetization/polarization $\boldsymbol{H_{cJ}}$ or induction $\boldsymbol{H_{cB}}$ is characterized as the x-intercept, while the remanent polarization $\boldsymbol{J_r}$ or remanent induction $\boldsymbol{B_r}$ as the y-intercept. A schematic of the second quadrant with the important values labeled is shown in Figure 1.9.

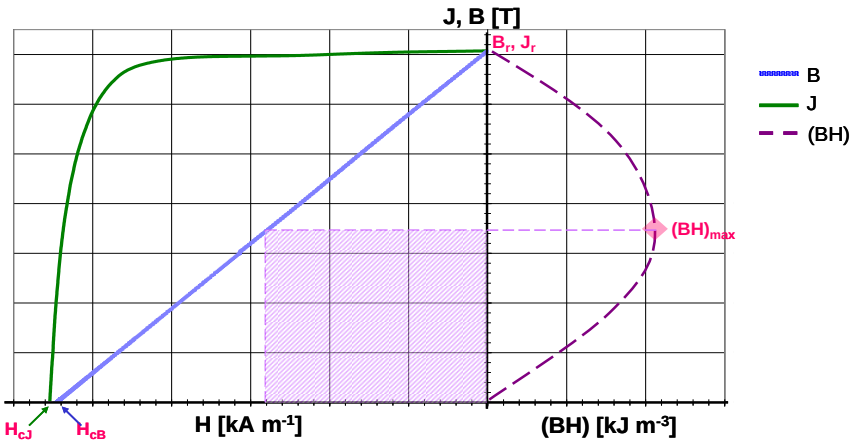

Figure 1.9. Second quadrant of the hysteresis loop and the calculated energy product displayed in the first quadrant. The x-axis of the first quadrant if the energy product (BH) and the second quadrant is the coercive field (H). The diamond marker indicates $(BH)_{max}$ and the shaded area represents the maximum power available.

Additionally, $\boldsymbol{M_s}$ can be found in the first and third quadrants. At points near $\boldsymbol{B_r}$, the demagnetization curve is considered reversible, with a slope μ_{rev}. In an ideal case, $\mu_{rev} = 1$ although in real magnets $\mu_{rev} > 1$.

The properties of hysteresis loops are governed by the extrinsic properties of the magnets, for instance the saturation magnetization/polarization, magnetic exchange, magnetocrystalline anisotropy of the magnetocrystalline phases, and the influence of the microstructure on the magnetic reversal process. For more effective magnets, a square-like $\boldsymbol{M(H)}$ hysteresis loop is desired. The squareness of the hysteresis loop can also be regarded as an indicator of how homogeneous a sample is with respect to the elemental distribution and microstructure. The squareness coefficient SQ (Eq. (24)), is the ratio of the actual area under the $\boldsymbol{M(H)}$ curve S over the ideal area in the second quadrant. SQ values closer to 1 indicate more ideal magnets.

$$SQ = S \Big/ M_r \cdot \boldsymbol{H}_{cM} \tag{24}$$

When examining $\boldsymbol{B(H)}$ curves, one ideally wants a linear plot in the second quadrant; this is indicative of a magnet which is stable during operation. If a shoulder appears in the induction curve, the behavior is non-ideal. Hard ferrites, for example NdFeB, Sm-Co, and other hard magnets possess generally straight induction curves. Also, strong permanent magnets have an intrinsic coercivity much larger than the remanence or the applied field corresponding to $(BH)_{max}$. This behavior is explained by the independence of $\boldsymbol{M}$ at values close to $\boldsymbol{H_{cM}}$, and illustrates why a square-like hysteresis loop is desirable for magnetic applications.

1.1.8.1 Coercive Field and Coercivity

The coercivity of a magnet is a measure of the stability and helps define whether a magnet is hard, semi-hard, or soft. Coercive fields related to the induction and magnetization may denoted by $\boldsymbol{H_{cB}}$ and $\boldsymbol{H_{cJ}}$, respectively. $\boldsymbol{H_{cJ}}$ is also referred to as the intrinsic coercivity, which reaches high values in rare-earth magnets due to the high intrinsic magnetocrystalline anisotropy. This is one of the characteristics making rare-earth magnets suitable for applications that require flat-shaped magnets. The difference between the coercive field and coercivity is that one is the magnetic field needed to reduce the magnetization to zero starting at an arbitrary magnetization level, while the other begins at saturation, respectively.

1.1.8.2 Saturation Magnetization

At the point of magnetic saturation $\boldsymbol{M_s}$, no further magnetization is possible. The value of $\boldsymbol{M_s}$ can be described by Eq. (25), where N is the number of atomic moments. This is the same as the total magnetic moment per atom, multiplied by the number of atoms present per unit volume.

$$\boldsymbol{M_s = Ng\mu_B J} \tag{25}$$

1.1.8.3 Remanent Magnetization and Remanence

When ferromagnetic materials are magnetized in a specific direction, the magnetization does not relax back to zero after the field is removed; however, some misaligned magnetic domains are formed (i.e. to reduce stray field). The result is a lower bulk magnetization. The remanence is a measure of magnetic strength, and is characterized by the flux density remaining after removal of a field once a sample is brought to the saturation magnetization. It is also characterized quantitatively as the y-intercept of the hysteresis loop. The relationship between $\boldsymbol{M_r}$, $\boldsymbol{J_r}$, and $\boldsymbol{B}_r$ in zero-field is shown in Eq. (26). The difference between remanence and remanent magnetization is that remanence is the remaining field after the magnet has been magnetized to saturation, whereas the remanent field is what remains after the removal of the external field at an arbitrary point.

$$\boldsymbol{B}_r = \boldsymbol{J}_r = \mu_o \boldsymbol{M}_r \tag{26}$$

1.1.8.4 Maximum Energy Product

The energy product of permanent magnets determines the maximum magnetostatic energy per magnet volume and is the product of $\boldsymbol{B}$ and $\boldsymbol{H}$ at any point along the hysteresis curve. The maximum energy product $(BH)_{max}$ is defined as the maximum possible product in the second quadrant; at what is called the maximum working point *P*. $(BH)_{max}$ is a key figure of merit for permanent magnets as it characterizes to a large degree the performance abilities of the magnet (Eq. (27)). In an ideal magnet, characterized as having a straight induction curve between $\boldsymbol{B_r}$ and $\mu_o \boldsymbol{H_{cB}}$, $(BH)_{max}$ is also equal to twice the potential energy of the external magnetic field over the magnet volume.

$$(BH)_{\max} = \tfrac{1}{4}\boldsymbol{B}_r \cdot \boldsymbol{H}_{cB} = \left(\frac{\boldsymbol{B}_r}{2}\right)\left(\frac{\boldsymbol{B}_r}{2\mu_o}\right) = \frac{\boldsymbol{B}_r^2}{4\mu_o} \tag{27}$$

In an ideal magnet the working point would be located at ½$\boldsymbol{B_r}$; however, in real cases, the induction curve is nonlinear and the maximum working point may be located at some other point along the curve. Steels from the early part of the 20th century had maximum

energy products of about 1 MGOe, hexagonal ferrites showed increased maximum products of approximately 3 MGOe and NdFeB magnets have shown the highest values at about 56 MGOe. Rare-earth permanent magnets have 8 to 15 times higher energy products than ferrites.

1.2 Diffusion

There are four primary means of diffusion through solids, each of which can be denoted by its respective diffusivity, seen below:

- lattice (bulk) diffusivity, D
- dislocation pipe diffusivity, D_d
- grain boundary diffusivity, D_{gb}
- surface diffusivity, D_s

The relative diffusivities can be regarded as follows:

$$D << D_d \leq D_{gb} < D_s$$

Grain boundary diffusion is typically 4-6 orders of magnitude higher than bulk diffusion, this difference gap closing as the temperature increases due to the activation enthalpy of grain boundary diffusion H_{gb} increasing at higher rates than that of bulk diffusion H.

1.2.1 Bulk (Lattice) Diffusion

Lattice (bulk) diffusion is a relatively slow process and is characterized by the diffusion length l presented in Eq. (28) [15], where t is the time.

$$l \propto \sqrt{Dt} \tag{28}$$

1.2.2 Grain Boundary Diffusion

Grain boundary (GB) diffusion plays a prevalent role in processes such as coble creep, sintering, diffusion-induced grain boundary movement, recrystallization and grain growth, as well as discontinuous grain growth. A schematic of the high-diffusivity paths for diffusion is shown in Figure 1.10.

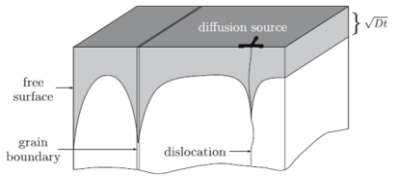

Figure 1.10. Schematic of high-diffusivity paths in a solid.[15]

In polycrystalline materials, GB diffusion is especially prevalent at temperatures below $T = 0{,}6T_m$. The grains boundary diffusivity follows an Arrhenius-like temperature dependence, as show in Eq. (29)[15], in which ΔH_{gb} is the activation enthalpy and D^o_{gb} is the pre-exponential factor for grain boundary diffusion.

$$D_{gb} = D^o_{gb} \exp\left(-\frac{\Delta H_{gb}}{k_B T}\right) \tag{29}$$

There are three dominant types of grain boundary diffusion behavior, which depend on the relative size of the diffusion length $\sqrt{Dt}$ with respect to the grain size d and grain boundary width δ:

- *Type A*: describes situations when diffusion annealing is performed at high temperatures and/or long times and/or in materials with small d. This requires that l be only slightly larger than the spacing between grain boundaries (Eq. (30)). For this regime, an effective diffusivity it used. This is determined by the relative fractions and diffusivities of the grain boundary and bulk phases.

$$\sqrt{Dt} \geq d/0{,}8 \tag{30}$$

- *Type B*: describes situations when the diffusion length after a given time t lies between δ and d Eq. (31)[15]. This is typically at lower annealing temperatures and shorter times, and/or in materials with larger grains. In this case, a more complex function is used, involving a triple-product of δ, D_{gb} and the segregation factor s (Eq.(32)[16]). x indicates the position.

$$s\delta < \sqrt{Dt} < d \tag{31}$$

$$s\delta D_{gb} = 1.322\sqrt{\frac{D}{t}}\left(-\frac{\partial \ln c(x,t)}{\partial x^{6/5}}\right)^{-5/3} \tag{32}$$

- *Type C*: describes situations when the diffusion length after a given t is small compared to δ (Eq. (33)[15]), and diffusion is essentially only feasible along the grain boundaries. The concentration-penetration curve in this case has a Gaussian profile, as in Eq.(34)[16] where c is the concentration, and c_o is the initial concentration.

$$\sqrt{Dt} < s\delta \tag{33}$$

$$c(x,t) = c_o \exp\left(-\frac{x^2}{4D_{gb}t}\right) \tag{34}$$

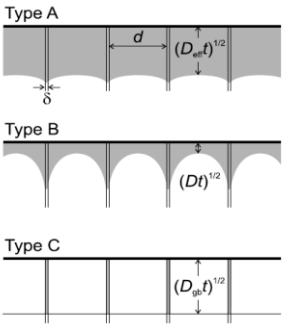

Figure 1.11. Schematic of A, B, and C diffusion regimes in a solid.[15]

The three diffusion regimes are represented schematically in Figure 1.11. The type of diffusion regime is also reliant on the temperature. It has been shown that in NdFeB materials at below about 900K ^{59}Fe grain-boundary diffusion occurs in the type-B diffusion regime, whereas Nd grain boundary diffusion follows trends in agreement with type-C diffusion[16]. At higher temperatures (above 900K), it is thought that a transition to the type-B regime may occur. Also, at temperatures near the melting temperature of the Nd-rich intergranular phase, both fast and slow grain boundary diffusion paths (through the liquid and solid grain boundaries, respectively) must be considered.

Upon assessing diffusion processes in materials, it is important to remember that bulk and grain boundary diffusion occur simultaneously. The *Le Claire parameter* β Eq. (35) is an indication of the extent to which grain-boundary diffusion is enhance with respect to bulk diffusion. Larger values of β indicate that the diffusion tail into a material will be more extensive (GB diffusion is more prevalent).

$$\beta \approx \frac{\delta D_{gb}}{2D\sqrt{Dt}} \tag{35}$$

Interdiffusion results when there are two diffusing atoms in dissimilar chemical environments, meaning that they have different chemical diffusivities. This process is used to describe the diffusion of Dy and Cu into the NdFeB magnets.

1.3 NdFeB Magnets

1.3.1 Basics of NdFeB Magnets

NdFeB magnets were first developed in the 1970s as a response to growing cobalt prices, and were presented as a viable alternative to Sm-Co magnets in 1984. They are practical from an economic perspective because iron is a very plentiful and cheap material, and neodymium is the most abundant of the lanthanides. Figure 1.12(a) shows a chronological comparison of the magnetic characteristics of several magnets.

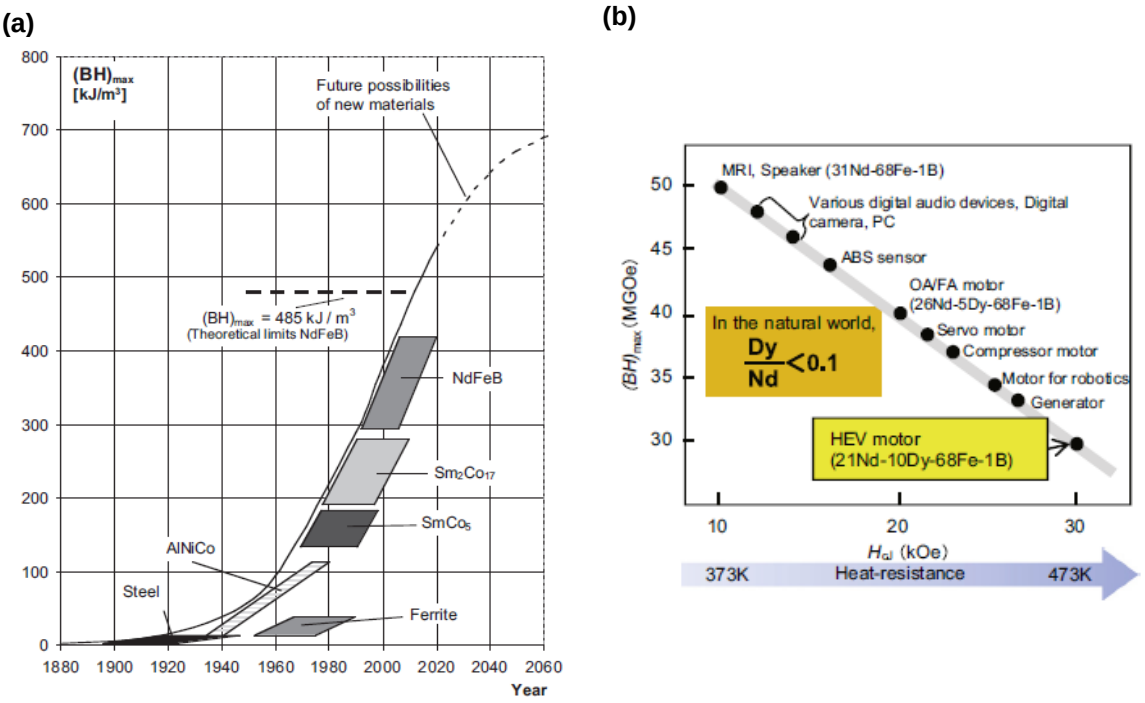

Figure 1.12. (a) Timeline of the maximum energy products for various permanent magnets[17] and (b) some commercial NdFeB applications[18].

NdFeB magnets are very widely employed due to their high energy product ($(BH)_{max}$ ≥ 450 kJ/m^3)[24]. Some of the most common applications include voice coil motors in hard-disk drives, motors (i.e. in hybrid and electric vehicles), generators, magnetic resonance imaging (MRI), and many areas in which increasingly compact devices are desired. Figure 1.12(b) shows some of the magnetic applications as well as a comparison between $(BH)_{max}$ and $\boldsymbol{H}_{cJ}$. China and Japan currently dominate the market in NdFeB magnets.

NdFeB magnets are able to reach magnetizations exceeding 1,4 T. The primary drawbacks to NdFeB magnets are low thermal stability and corrosion resistance. This may be improved through alloying or the addition of coatings, as will be addressed later.

1.3.2 Primary Phases of NdFeB Magnets

The main phases prevalent to NdFeB sintered magnets are outlined below. The pertinent area in the NdFeB phase diagram is also seen in Figure 1.14.

Φ-phase ($Nd_2Fe_{14}B$) – The hard magnetic phase of NdFeB sintered magnets is comprised of a tetragonal crystal structure ($P4_2/mnm$[20]) with a single-axis, positive crystal anisotropy. The Curie temperature is about 310 °C, meaning it is considered suitable for many practical applications[21]. The boron atom changes the dimensions of the unit cell from a cubic to a tetragonal structure, increasing in the anisotropy field. The magnetic moment of the Nd atoms act parallel to that of the iron. Figure 1.13 shows a schematic of the magnetic microstructure and the unit cell of the $Nd_2Fe_{14}B$ phase. Each unit cell is comprised of four formula units[20].

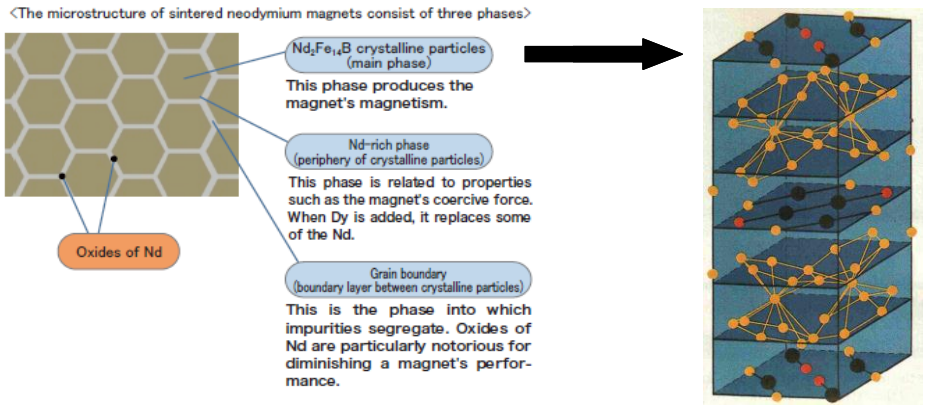

Figure 1.13. Microstructure of NdFeB magnets[22] and a schematic of the repeat cell of the $Nd_2Fe_{14}B$ phase comprised of 56 Fe (yellow), 8 Nd (black) and 4 B (red) atoms[23].

Nd-rich phase – The Nd-rich phase has a relatively low melting point of 670 °C and is paramagnetic at room temperature[21]. This phase may occupy as much as 5% of the magnet and plays a key role in the sintering process by enhancing densification of the magnet, thus increasing the physical and magnetic density of the magnet. During sintering, the liquid phase contributes to an increase in coercivity by enhancing the decoupling of magnetic grains and cleaning the surface of the hard-magnetic grain in order to deter the formation of nucleation sites for reverse domains. Due to the affinity of Nd for oxygen, NdO may form and hinder the diffusion of other atoms in this phase. This affinity is also the reason for the innately low corrosion resistance of the magnets.

η-phase ($Nd_{1.1}Fe_4B_4$) – This is a paramagnetic, boron-rich phase. It is also witnessed in between hard magnetic grains, and is desired as a finely dispersed phase. At the peritectic melting point, this phase separates into a liquid Nd-rich phase and α-Fe phase. The α-Fe phase can be detrimental to the coercive field and should be avoided[21].

Agglomeration of the η-phase (and hence α-Fe) can be reduced by quenching the magnet after sintering occurs, in order to pass through the peritectic point as quickly as possible.

Impurities – The primary impurity present in NdFeB magnets is the Nd-oxide, which is introduced during the manufacturing process. Such impurities cannot be removed after magnet formation and can prove detrimental to magnetic properties. Oxides are avoided through controlling the processing atmosphere during formation.

1.3.3 **Formation of Sintered NdFeB Magnets**

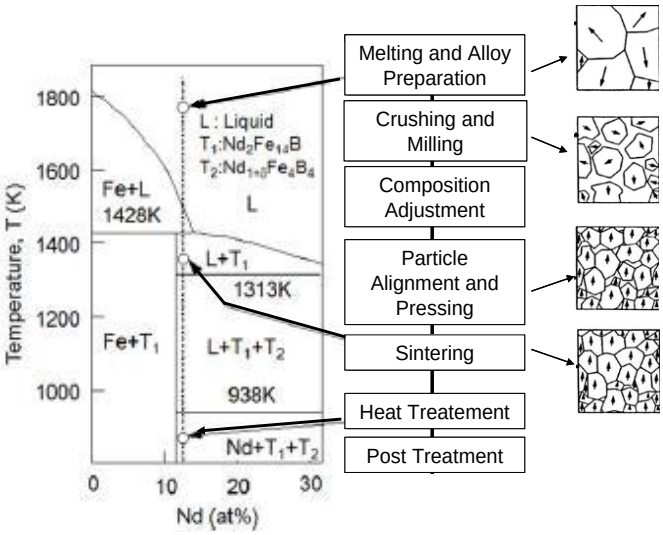

Figure 1.14. Processing steps for the creation of NdFeB magnets. Adapted from [24].

The majority of NdFeB magnets are created through powder metallurgy techniques. The basic steps are shown in Figure 1.14. First, Fe and B are melted together in an alumina (Al_2O_3) crucible, the atmosphere is degassed, and brought up to a temperature above the Fe-B liquidus temperature, at which point Nd is added. The amount of Nd used is typically higher than the stoichiometric proportion of the $Nd_2Fe_{14}B$ phase. Upon rapid cooling, an Nd-rich eutectic regions around the grain boundaries of the material results; these have a special purpose in the sintering process[10].

The ingots are then formed into rough powders via means such as hammer milling or hydrogen decrepitation and further refined via jet milling, ball milling, or mortar grinding. After being aligned in a magnetic field, the powder is isostatically pressed to form a compact powder. Sintering is then performed to complete densification of the magnet, reaching about 99% of the theoretical maximum density and achieving a high energy

[10] The fracture micromechanism in NdFeB magnets is intergranular fracture. Increasing the proportion of Nd-rich phase has been shown to increase the fracture toughness and impact stability of the magnets because of its good deformability[26].

density. During sintering, the sample is brought to a temperature between the Nd-liquidus temperature and the melting point of the hard magnetic phase, making mass transport of the Nd-rich phase possible and eliminating voids in the material.

Thermal treatment of the magnets is generally employed in order to optimize magnetic properties. Often, a two-step heat treatment is used, the first annealing at higher temperatures (700-900 °C), and the second at lower temperatures (500-600 °C). Figure 1.15(a) shows the microstructure before and after post-annealing treatment. It has been shown that fast-quenching after the treatment should be employed to increase the hysteresis loop squareness and optimize the coercivity[25]. The stresses induced during quenching are relieved during the low-temperature aging process. Ideally, some net-shape forming technique is used so that post-sintering machining is kept at a minimum. Shaping after sintering is usually done via electric-spark machining and grinding due to the brittleness of the material[26].

1.3.4 Ideal Magnetic Structure and Post-sintering Treatment

Properties such as the amount of each phase present in the magnet as well as the microstructural relationship between phases are largely determined by the processing parameters and dictate the magnetic properties of a material. If the correct experimental parameters are employed, the microstructure of the NdFeB magnets can be tailored in order to achieve highest H_{cJ} and B_r values, as well as increase the squareness of the hysteresis loop. The two dominant means of changing the microstructure are:

- Optimizing processing parameters (i.e. fabrication technique, heat treatment)
- Alloying with additional elements (i.e. Cu, Co, Al Ga, Ni, Ti)

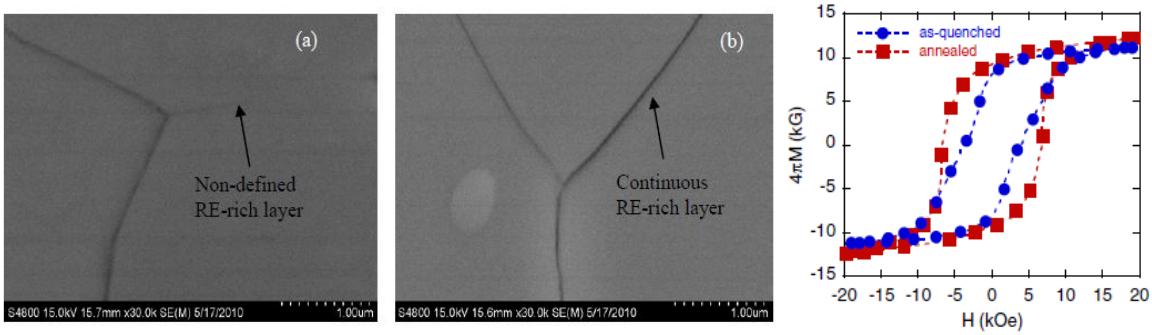

Figure 1.15. FEG-SEM images showing grain boundary after heat treatment for an NdFeB magnet (a) is the sample after sintering and (b) is after heat treatment. Additionally, the hysteresis loops before and after treatment are shown.[27]

The coercivity in NdFeB magnets is heavily governed by the microstructure formed during sintering and post-production treatment. Directly after sintering, the grain boundary formed

by the solidification of the Nd-rich phase may be discontinuous and non-uniform. By annealing the sample at optimum time and temperature, the grain boundary can be made smoother and more uniform, leading to increased decoupling of the hard magnetic phases and a higher coercivity[9, 28, 29,30] (Figure 1.16)[11]. Additionally, in order to correct for a small coercivity in the surface grains of NdFeB magnets and reduce the number of potential reverse-domain nucleation sites, Nd coatings have been applied to the magnet surface followed by annealing[28].

Ideally, the grain size of the magnets should be small; this helps retard the spread of reverse domains throughout the system[12]. Material grain size may be tailored to some extent by controlling the particle size of powders used in forming the magnets.

The guiding principles for optimizing the microstructure include[24,31]:

1. Reducing the grain size of the $Nd_2Fe_{14}B$ phase to decrease the likelihood of a multi-domain structure
2. Controlling the interfacial microstructure between the $Nd_2Fe_{14}B$ phase and the Nd-rich phase
3. Enhancing the degree of magnetic isolation of each grain
4. Concentrating heavy rare earth alloying elements such as Dy and Tb near the grain boundaries

1.3.5 Alloying Additions

The addition of alloying elements to NdFeB magnets has improved the magnetic properties, especially when performed in conjunction with proper heat treatments. As a general trend, high melting-point metals (Zr, Nb, V, Mo, Ti) are used to achieve a refined grain structure because the metal atoms serve as nuclei for crystallization, resulting in a high nucleation frequency and less grain growth. Low melting-point metals (Cu, Al, Ga, In, Zn) encompass the magnetic grains during crystallization and impede reverse domain growth. Elements which influence the intrinsic coercivity of the magnets do so by partially substituting one of the elements in the $Nd_2Fe_{14}B$ lattice. For instance, heavy rare earth elements (HREEs) (i.e. Pr, La, Dy, Tb, Sm) substitute Nd, transition elements (i.e. Co, Mn) substitute Fe, and C substitutes B[32].

[11]Because the nucleation of reverse domains is responsible for demagnetization of NdFeB magnets[9], achieving magnetic (de)coupling of the main phases is very important in order to increase sample coercivity. See 1.1.6.1 Bloch Walls and Nucleation Mechanisms.

[12]NdFeB magnets have a nucleation-based spreading of reverse domains, meaning that once a reverse domain penetrated a grain, it passes through rather easily. Decreasing the size of grains limits this as reverse domains are then caught at grain boundaries.

1.3.5.1 Dysprosium Additions

The maximum energy products of NdFeB magnets without RE addition has reached $(BH)_{max}$ = 50 MGOe, obtained by alloying with Cu and Al. However, the coercivity of these magnets is only 12 kOe, which is too low for applications such as hybrid and electric motor vehicles[9]. Additionally, the operating temperatures of NdFeB magnets in applications such as hybrid motors can reach temperatures of up to 473 K (200 °C)[18] while also being exposed to high demagnetizing fields. At temperatures above the Curie temperature of NdFeB magnets, thermal degradation of the magnet occurs. The coercivity and feasible operating temperature of the magnets has been increased via the selective introduction of HREEs such as dysprosium (Dy) and Terbium (Tb). However, because Tb is much more expensive than Dy, it is impractical for use in commercial applications[18].

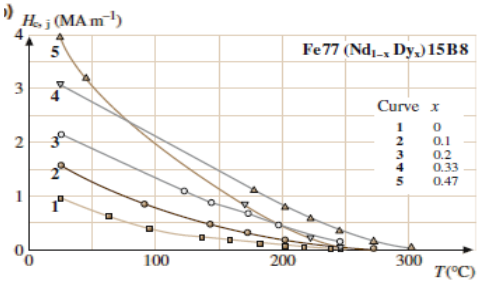

Figure 1.16. The effect of Dy additions on H_{cJ} at various temperatures.[5]

The intrinsic coercivity and the Curie temperature (thus the temperature stability) are increased by incorporation of Dy atoms into the hard magnetic grains in the $Nd_2Fe_{14}B$ lattice (Figure 1.16; note an increasing temperature dependence with increasing Dy content). The resulting $Dy_2Fe_{14}B$ cells have the same crystal structure as the $Nd_2Fe_{14}B$ cells[33]; however, they have a higher crystal anisotropy, leading to a higher coercive field (H_A = 15,0 T for $Dy_2Fe_{14}B$ and H_A = 7,6 T for $Nd_2Fe_{14}B$[34]). A linear relation between the degree of atom substitution and the increase in coercivity has been observed[13, 35]. Dy inclusion has also been shown to increase the impact stability in NdFeB magnets[26].

The magnetic moments of Dy are antiferromagnetically coupled to those of Nd[36] in the $RE_2Fe_{14}B$ lattice, leading to a reduction of $\boldsymbol{M_s}$ and $\boldsymbol{B_r}$. This effect can be clarified by considering the anisotropy energy and exchange interaction (see sections 1.1.5 and 1.1.3, respectively). The latter relies on the orientation of magnetic moments being a function of the distance between atoms. Shandong, et al.[32] have calculated that in the $Nd_2Fe_{14}B$ phase, $J_{12} > 0$ if iron atoms are more than 0,250 nm apart, resulting in ferromagnetic coupling. The distance between Fe atoms in the $RE_2Fe_{14}B$ lattice varies between 0,209 and 0,382 nm, meaning that the substitution of the larger Nd atom (r_{Nd} = 0,264 nm) with the smaller Dy atom (r_{Dy} = 0,249 nm), results in a reduction in iron atom distance and thus antiferromagnetic coupling. By confining the HREEs to the peripheral of the hard magnetic grains, the losses in $\boldsymbol{B_r}$ can be minimized.

Another concern of incorporating Dy is the scarcity of resources: the natural abundance of Dy is less than 1/5 that of Nd[24] (other sources report even higher disparities). Applications such as hybrid motors can require coercivities of up to 2387 kA/m (30 kOe): this corresponds to a 10 wt% substitution of Dy for Nd in the magnet[18]. However, for 30 kOe commercial sintered magnets currently used in motor applications, Dy is substituted for 40% of Nd[9]. Researchers looking to create innovative devices with sustainable technology have hence been searching for production methods which introduce only the minimum amount of Dy necessary into the system. Such methods are favorable based on both scientific and economic merits.

1.3.5.1.1 Application via Annealing

Dysprosium has been introduced into NdFeB magnets both during and after the sintering process. One of the primary concerns of introducing the HREEs during the sintering process is that the amount of material being used exceeds optimal amounts, leading to the wasting of scarce and expensive materials. If higher than optimal quantities of Dy are present, the atoms will diffuse into the hard grains at distances further than necessary, in addition to agglomerating to form Dy-rich zones within the sintered magnets. The introduction of Dy into the magnet after sintering, by coating application and an annealing treatment, may yield a more desired microstructure by better confining the HREEs to the grain peripherals and boundaries. The introduction of Dy and other HREEs during an annealing process is commonly referred to as 'grain boundary diffusion (GBD) treatment', as well as several similar names. These have been shown to be promising techniques for increasing $\boldsymbol{H_c}$ of the magnet while decreasing losses in $\boldsymbol{B_r}$ [18] (Figure 1.17).

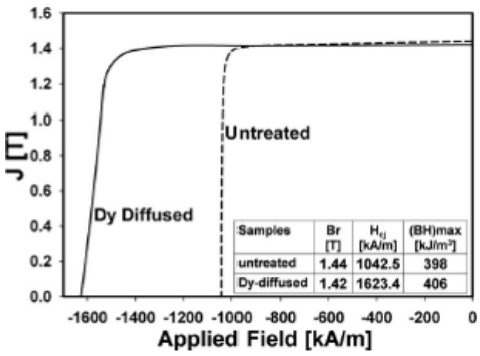

Figure 1.17. Demagnetization curves comparing Dy-diffusion processed and untreated samples.[10]

Confining Dy to the grain boundary results in:

- An increase in coercivity and reduced likelihood of reverse domains forming at the grain boundaries
- A reduction of Dy substitution for Nd in the hard metallic phase, meaning lower magnetization losses
- A reduction in the amount of Dy required for a desired coercivity, resulting in savings in materials and cost

1.3.5.1.2 The Annealing Process

When being incorporated after sintering, the Dy is most commonly applied as a coating to the magnet surface, either as the pure metal[12, 36], or part of a compound such as**,** Dy-Ni-Al[18], Dy_2O_3[11], DyF_3[9, 11, 13, 37, 38, 39], DyCu, DyGa and Dy_3Co alloys[12] as well as DyH_x hydride[12] and as a Dy-F solution[40]. Coatings have been applied both as a powder [9, 12, 18] by means such as dipping[38, 39] and painting, as well as methods such as sputtering [36, 43, 44], electrophoretic deposition[38], vapor deposition[10,45], or as a vapor at the magnet surface during annealing[46].

The group of Popov, et al.[12] has experimented with the inclusion of Dy into NdFeB systems via the application of metallic powders. The materials applied included DyCu, DyGa, and Dy_3Co alloys, as well as DyH_x (x = 2,0 – 2,2) hydride. One of the reasons for testing intermetallic compounds is that HREE oxides and fluorides are stable chemical compounds displaying high melting temperatures, which also require high activation energies before being able to decompose and diffuse through the sample. The melting points of the intermetallic compounds did not have a noticeable effect on the diffusion processes. Rather, it was more important that the annealing temperature be above the eutectic for to achieve a liquid Nd-rich phase, although the Cu-containing compound became sintered to the magnet at such temperatures. Employing such intermetallic compounds (those with Cu, Ga, Co) can also lead to an increase in corrosion resistance, coercive force, and thermal stability[42].

Generally speaking, after being coated the magnets are annealed at up to 1000 °C, above the melting point of the Nd-rich phase (670 °C), where they are held in order for the Dy to diffuse through and incorporate into the magnet. There is also commonly a second heat treatment, during which the magnets are held at a lower temperature (around 500 - 600 °C) for a short amount of time (1 - 3 hrs) in order to relieve stresses and interfacial energy[47]. The formation of the magnetic structure in Dy-NdFeB magnets occurs in two primary steps:

1. Dysprosium first undergoes grain boundary diffusion, traveling through the (liquid) Nd-rich phase. This is a fast, diffusion-controlled process, the speed of which is also believed to be related to the thickness of the applied coating. Dy has a stronger affinity with oxygen than with neodymium[9], so in order to allow for the easy diffusion of Dy throughout the grain boundaries, it is especially important to inhibit the inclusion of diffusion-hindering oxides during the production process[22].

2. During bulk diffusion/substitution, Dy is incorporated into the edge of the $Nd_2Fe_{14}B$ grains via the substitution of Nd for Dy to create a $(Nd, Dy)_2Fe_{14}B$ rim. This is a slow process, which is responsible for the reduction in B_r seen at higher annealing times. The coercivity has been observed to increase monotonically with time during this process[12]. The Nd driven out of the grains is then located in the Nd-rich phase or as the Nd-O phase in grain boundaries or at the surface[37]. A schematic of the ideal structure after diffusion annealing is shown in Figure 1.18.

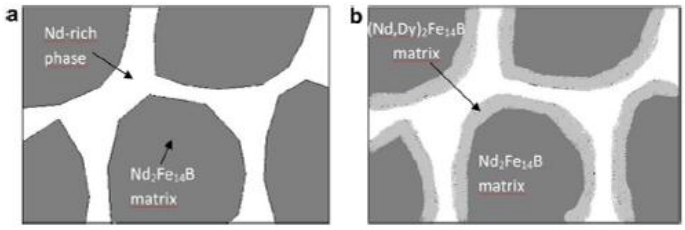

Figure 1.18. Schematic showing the NdFeB magnet (a) before and (b) after GBD with Dy.[38]

1.3.5.1.3 Benefits and Drawbacks of GBD of Dy

A process called High-anisotropy Field Layer (HAL) method uses GBD to incorporate Dy into NdFeB magnets[22]. Currently, magnets with the hard phase making up 97% of the magnet are able to be produced. In the lab, magnets with $(BH)_{max}$ of 59 MGOe have been achieved, while in practical applications this has reached up to 55 MGOe. Additionally, magnets created using the HAL process are able to achieve B_r of 3-5% higher than other methods while employing 20-50% less Dy.

By incorporating Dy into the magnet via GBD, the amount of HREE necessary to bring about a defined increase in coercivity may be reduced, requiring as low as only 0,5 wt% Dy (applied in the grain boundary phase throughout the magnet) rather than 5% (distributed throughout the entire magnet), while retaining higher remanent magnetizations[21]. GBD processes have been found to use less than 10% as much Dy as the two-allow method, while achieving the same coercivity values[9]. The Dy at the edge of the hard magnetic grains forms a rim of $Dy_2Fe_{14}B$, which has a higher crystal anisotropy/coercivity and acts somewhat like a shield, retarding the formation of reverse domains. A comparison of the grain boundary structure in samples where Dy was introduced during annealing and via the binary alloy method is seen in Figure 1.19.

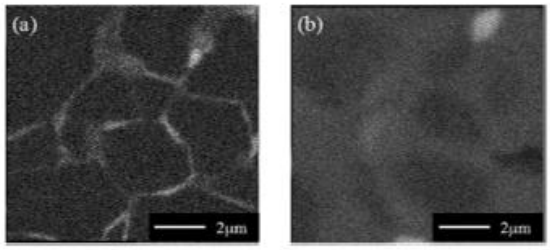

Figure 1.19. Compositional images of NdFeB magnets produced using (a) GBD method and (b) binary alloy method.[9]

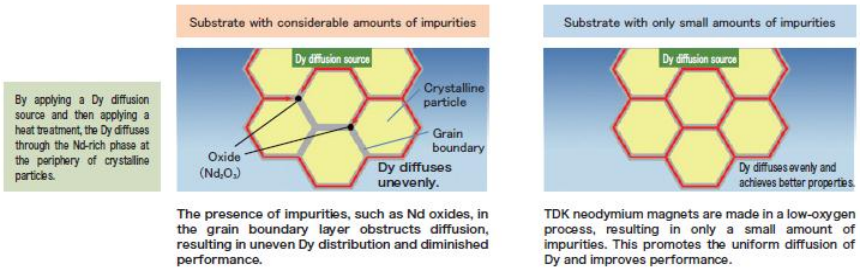

Figure 1.20. Diffusion of Dy through the NdFeB magnet.[22]

Schematics of Dy-diffusion through magnets that contain defects at the grain boundaries can be found in Figure 1.20. Additionally, Li et al.[9] have found that oxides are concentrated in the Nd-rich phase. Also, adjacent to the hard-magnetic shell, there is a thin layer of Nd, thought to be that which is rejected from the $(Dy, Nd)_2Fe_{14}B$ grain.

If the microstructure of the magnet before sintering is optimized and a continuous grain boundary exists, the Dy will be able to diffuse further into the magnet[37]. The homogeneity of the Dy distribution can be witnessed by the squareness of the hysteresis loop: a high squareness is indicative of a more homogeneous sample[18]. Improvements in coercivity and high hysteresis-loop squareness have been witnessed at depths of up to 5 mm[18] using GBD processes.

Because the magnetic moment of Dy in $Dy_2Fe_{14}B$ acts antiparallel to the magnetic moment of the iron atoms, increasing the thickness of the substituted region along the grain border results in a decrease in B_r (Figure 1.21); however, if the layer is kept sufficiently thin, B_r does not decrease significantly. If the sample is retained at high temperatures (up to a limit), the Dy will diffuse further into the material until it becomes homogenized along the shell of the hard magnetic grain (no GB enrichment)[10, 34].

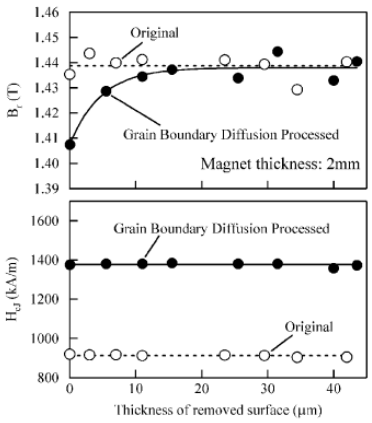

Figure 1.21. B_r and H_{cJ} profile of a magnet using GBDP. [11]

The disadvantage of using GBD with NdFeB magnets is that the diffusion distances are relatively small; as the magnet thickness increases, gains in coercivity are reduced due to the limited diffusion of Dy throughout the material[18]. This confines the application of such techniques to magnets with small thickness[48]. Based on the experiments of Soderžnik et al.[38], about 10 hours is needed to achieve the optimal coercivity in a 3,0 mm sample NdFeB sample coated with Dy. At longer times, the coercivity could be increased by only 5-10%. The implication for this is that for industrial applications, the GBD process is economically feasible only for samples up to 3 mm thick. However, Oono et al.[18] reported that Dy, when

applied as part of a Dy-Ni-Al powder mixture painted to the surface, was found in the grain boundary phases at up to 3 mm, meaning that if painted on both sides, it should be able to diffuse to the center of a 6 mm thick magnet.

Sepehri, et al.[10] have investigated the addition of Dy into NdFeB magnets. Dy coatings were applied using vapor deposition at 900 °C, then aged for an hour at 500 °C. The resulting B_r was found to be almost equal to those before the diffusion process, with a 56% increase in coercivity from 1043 kA/m (13,1 kOe) to 1623 kA/m (20,4 kOe). The untreated sample displayed discontinuous Nd-rich phase, while the treated samples displayed a thicker, more continuous GB network. This enhancement of the grain boundary microstructure was due to the expulsion of Nd from the $(Dy, Nd)_2Fe_{14}B$ grains as Dy substitution for the Nd in the hard magnetic grains progressed; the only place for displaced Nd-atoms to go was the grain boundary. Within the grain boundary phase, Dy was not strongly partitioned, as witnessed in Figure 1.22 from Komuro, et al. The Nd-rich channels (a few nanometers[9] thick) served not only as a pathway for the diffusion of Dy atoms, but also improved the decoupling of the hard magnetic grains. Near the sample surface, energy filtered Nd and Dy maps showed no enrichment of Dy at the grain boundaries, indicating a homogeneous dispersion of Dy in the $(Dy, Nd)_2Fe_{14}B$ and in the grain boundary. Conversely, at the center of the sample the grain boundary was still found to be Dy-rich. Similar observations have also been obtained by Li[9] and Popov[12].

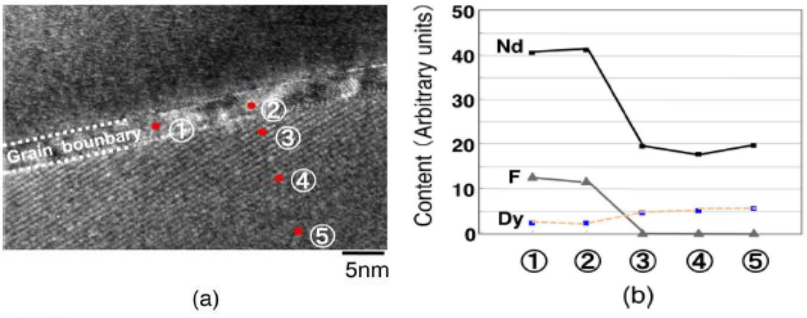

Figure 1.22. (a) Bright field image and (b) corresponding composition of an NdFeB magnet using GBD[40].

1.3.5.2 Copper Additions

Copper has been incorporated into NdFeB magnets as a means of increasing the coercivity, energy density, corrosion resistance[5], and working temperature of the magnets by enriching the Nd-rich phase[5, 9, 10]. The additions lead to the formation of compounds such as RECu (which has a reduced melting point)[49], which encompass the magnetic grains and lead to a refined microstructure. The growth of reverse domains is consequently impeded. However, Cu has been found to decrease B_r and T_c[49].

Small amounts (as low as 0,02%) of Cu added to (Nd, Dy)FeB alloy increased H_{cJ} without B_r reductions[50], thus increasing the working temperature ~25 °C. Small Cu additions (up to 0,15%) to (Nd, Dy)(Fe, Co)B systems also increased B_r and H_{cJ}, overcoming the decrease in H_c that results from Co addition to the system and increasing the operating temperature by about 75 °C. The joint addition also increased the corrosion resistance. At additions over 2% Cu both B_r and H_{cJ} decreased.

Cu is most commonly applied to NdFeB magnets as part of a powder compound, for instance with dysprosium as DyCu. However, at annealing temperatures above 800 °C, DyCu powders applied to NdFeB magnets became sintered to the magnet during heat treatment due to the low melting point of the compound[12]. Another drawback to using DyCu powders is the difficulty in obtaining fine powders due to the high mechanical strength**.** Figure 1.23 shows the Dy-Cu and Nd-Cu phase diagrams.

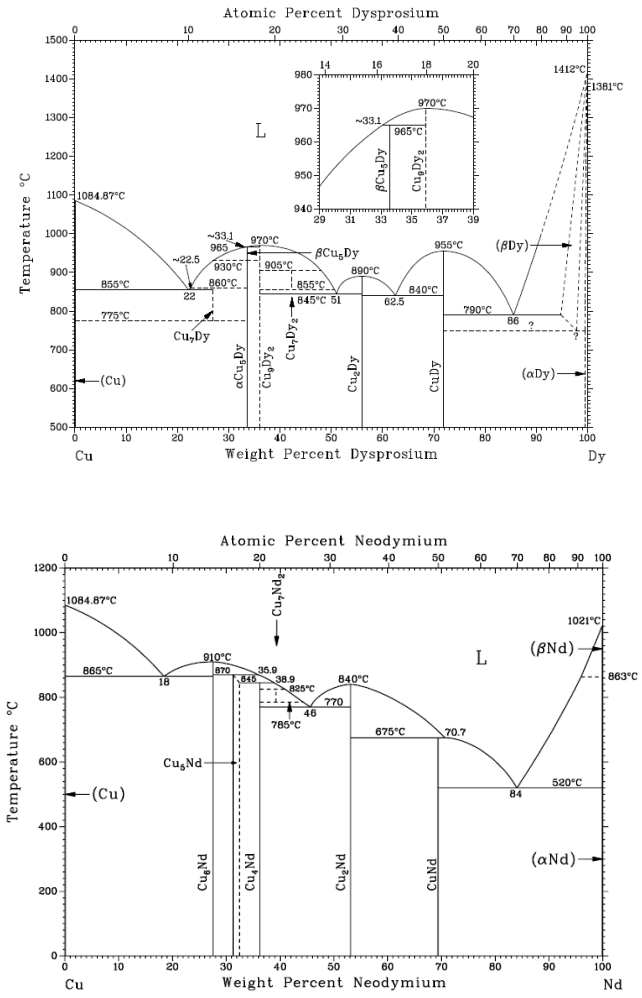

Figure 1.23. Phase diagrams for the Cu-Dy (top) and Cu-Nd (bottom) systems.

Chapter 2 - Experimental Method

2.1 Specimen Preparation

Several magnets with dimensions 10mm x 10mm x 3mm, containing various amounts of Dy, were procured (Table 2.1). Samples with a lower initial amount of Dy of 0,5% are referred to as ‘lowDy’, and those with a higher initial content of 4,5% as ‘highDy’. Coatings of Dy and/or Cu were applied using physical vapor deposition (PVD). After coating deposition, a 10 nm layer of TaN was applied to the magnet surface in order to shield against oxidation. Samples were stored to an argon environment.

Table 2.1. Properties of procured magnets.

Series	Mass % Dy
LowDy	0,5 %
HighDy	4,5 %

2.1.1 Pure-Dy Coatings

Double-sided coatings of pure Dy were applied to lowDy magnets, with the thickness applied to each side being 1 µm, 2 µm, 5 µm, 10 µm, or 20 µm thick. Additionally, coatings were applied to the highDy magnets on both sides, with the thickness applied to each side being 1 µm, 2 µm, 5 µm or 10 µm. Coatings of 20 µm were also applied to the lowDy and high magnets on one side. Table 2.2 presents the calculated values for the percent Dy included in the magnet for lowDy and highDy samples with coatings applied in both single- and double-sided manners.

Table 2.2. Dy coating thicknesses applied to magnets and the corresponding wt% Dy.

Coating thickness, t	Wt% Dy, total			
	Single-sided		Double-sided	
	lowDy	highDy	lowDy	highDy
1 µm	--	--	0,575	4,571
2 µm	--	--	0,659	4,642
5 µm	--	--	0,897	4,854
10 µm	--	--	1,291	5,205
20 µm	1,291	5,205	2,070	--
	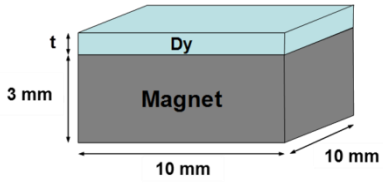		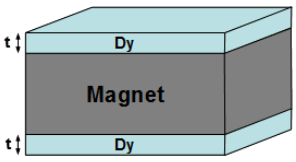	

2.1.2 Dy-Cu Coatings

Layered coatings of Dy and Cu were applied on both sides of lowDy and highDy magnets. The layer thicknesses were chosen in order to obtain a specific wt% Cu in the magnet and a specific relative composition of Cu and Dy in the coating system. Copper coatings were applied in order to obtain 0,5 wt%, 0,3 wt% and 0,1 wt% Cu in the magnet. The amount of Dy was then calculated for each quantity of copper in order to have 22,5 wt% Dy in the coating, corresponding to the Cu-rich eutectic. Using the previously calculated Dy thicknesses, the amount of Cu needed to have a coating composition consistent with the Dy-rich eutectic (86 wt% Dy) was determined. A summary and schematic is found in Table 2.3. During the application of the 0,5 wt% Cu magnet with a Cu-rich eutectic coating, the Cu sputtering target was depleted, and the coating could not be completed. Changes are reflected in the table.

Table 2.3. Resulting mass % Dy and Cu in lowDy and highDy magnets after coating.

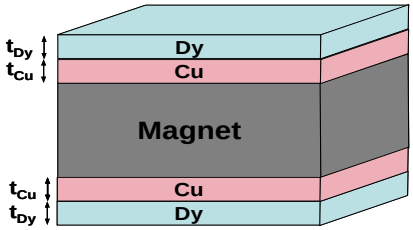

			Mass % Total			Thickness, $t_{Cu,\ Dy}$ [µm]	Mass % in Coating
			0 initial	lowDy	highDy		
Cu-rich eutectic 22 wt% Dy in coating	0,5 wt% Cu (Side 1)	Cu	0,429	0,429	0,429	6,362	78
		Dy	0,139	0,639	4,639	1,880	22
	0,5 wt% Cu (Side 2)	Cu	0,429	0,429	0,429	4,581	72
		Dy	0,141	0,641	4,641	1,880	28
	0,3 wt% Cu	Cu	0,300	0,300	0,300	3,823	78
		Dy	0,085	0,583	4,567	1,130	22
	0,1 wt% Cu	Cu	0,100	0,100	0,100	1,272	78
		Dy	0,028	0,528	4,522	0,376	22
Dy-rich eutectic 88 wt% Dy in coating	0,0283 wt% Cu	Cu	0,023	0,023	0,023	0,292	14
		Dy	0,141	0,640	4,634	1,880	86
	0,0140 wt% Cu	Cu	0,014	0,014	0,014	0,176	14
		Dy	0,085	0,584	4,580	1,130	86
	0,0046 wt% Cu	Cu	0,005	0,005	0,005	0,058	14
		Dy	0,028	0,528	4,527	0,376	86

2.2 Heat Treatment

Annealing treatments at various times and temperatures were performed. The samples were inserted into a quartz tube, which was then flushed several times with argon and put under a vacuum. A Carbolite furnace was used for the annealing treatments. A schematic and photograph of the oven set-up can be seen in Figure 2.1. A fan was used to increase the cooling rate of the sample after removal from the furnace. The initial vacuum was produced using a Leybovac PT 150/4, and a high vacuum was achieved using a Turbotronik NT 150/360. The pressure was monitored using a Leybold-Heraeus Combitron OM330.

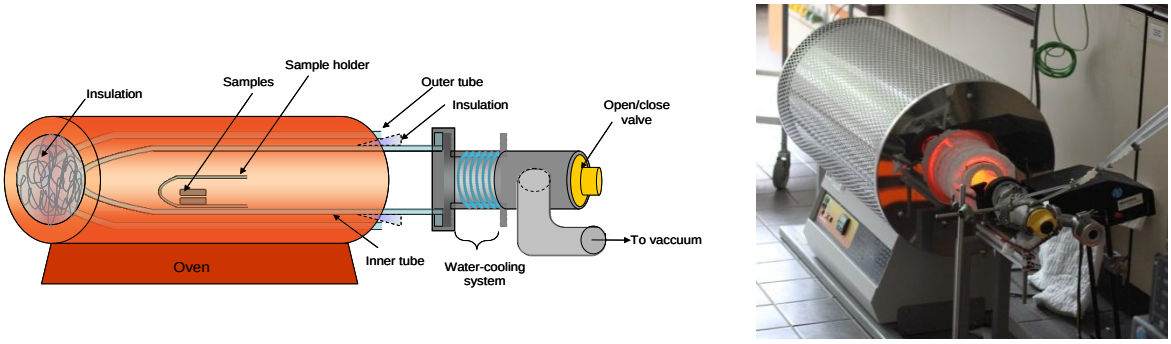

Figure 2.1. Schematic and photograph of the annealing conditions.

2.2.1 Annealing in Argon

Samples of coated lowDy magnets were annealed at 900 °C in one-hour intervals, for a total time of 4 hours. The magnets were places inside the sample holder (a small quartz tube), without any casing and in an argon atmosphere. After each hour, the samples were removed from the oven and allowed to cool, after which the magnetic properties were measured in order to track the process of Dy diffusion into the material. Once the measured coercivity reached a plateau, no more annealing cycles were performed. A final low temperature annealing was performed at 500°C for 1 hour.

2.2.2 Annealing in Vacuum

Samples of lowDy and highDy magnets underwent cycles consisting of two steps: a high temperature (HT) annealing at 900°C for 1 hour, followed by a low temperature (LT) annealing at 500°C for 1 hour. Each combination of a HT and LT anneal is referred to as one annealing cycle. The samples were packed into a Mo casing in order to prevent the loss of Nd from the magnet during the high-temperature phase. After each cycle, the magnetic properties of the magnets were measured. A reference (uncoated) sample was also annealed in these trials.

2.3 Magnetic Characterization

Hysteresis curves were generated using a Metis Capacitive Discharge Magnetizer in conjunction with a Metis HyMPulse hysteresis meter for hard magnetic materials. This device allows one to measure the magnetic properties of a magnetic material, regardless of geometry. The device consists of the following parts:

- CDMM magnetizer 28 kJ 3kV
- CDM coil and probe
- Signal processing unit
- PC with data acquisition card and software
- Cooling unit

The magnetic coil and probe consist of an axial coil with a cylindrical aperature, which generates a peak field of 7 T with a pulse duration of 20 ms. Background and positioning may be compensated for in this system. There is a probe for $\boldsymbol{M}$ and $\boldsymbol{H}$, as well as a flux diagnostic sensor. Post data processing is used to produce values for $\boldsymbol{H_{cB}}$, $\boldsymbol{H_{cJ}}$, $\boldsymbol{B_r}$, $\boldsymbol{B_m}$, $\boldsymbol{H_m}$, $(BH)_{max}$, and $\boldsymbol{H_{knee}}$. The device consists of a CDMM capacitor discharge magnetizer and a data acquisition unit. A ThermoFlex 1400 cooling apparatus was used to maintain the coil temperature in the vicinity of 30°C.

Figure 2.2 Metis Discharge Magnetizer and HyMPulse hysteresis meter.

2.4 Microstructural Characterization

Backscattered electron (BSE) images were collected using a JEOL JXA 8900 scanning electron microscope (SEM) at the Siemens AG facilities in Munich. Compositional analysis was performed using wavelength dispersive x-ray analysis (WDX). An image of the SEM is provided in Figure 2.3.

Figure 2.3. JEOL JXA 8900 SEM device.[53]

Chapter 3 - Results

3.1 Reference Samples

Found in Table 3.1 are the properties of the reference (as-received) magnets. Magnets containing higher amounts of Dy had a higher H_{cJ} but a lower B_r and $(BH)_{max}$.

Table 3.1. Initial properties of the reference samples.

	H_{cJ} [kOe]	B_r [kG]	$(BH)_{max}$ [MGOe]
lowDy	13,46	13,66	44,96
highDy	22,85	12,85	40,80

3.2 Pure Dy Coatings

3.2.1 Coating Assessment

The coatings of Dy were checked for uniformity and agreement with the intended thicknesses using SEM imaging. Coatings appear to have a columnar-like structure and met the thicknesses intended during PVD application. Figure 3.1 shows images taken of lowDy samples coated with 1 µm, 5 µm and 20 µm of pure dysprosium. The coatings appear to adhere well to the surface and are relatively even.

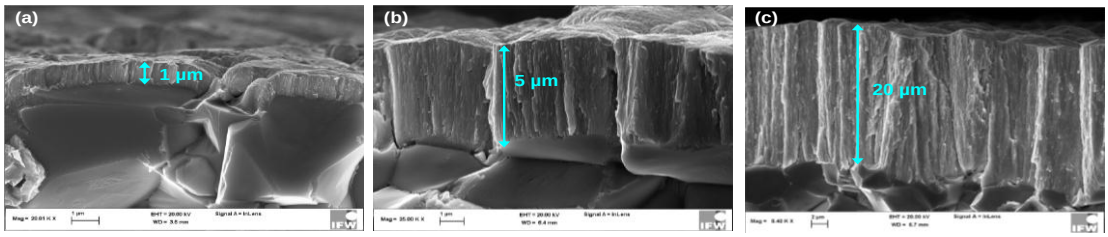

Figure 3.1. SEM images of Dy coatings with thicknesses (a) 1 µm, (b) 5 µm and (c) 20 µm.

3.2.2 Coatings and Magnetic Properties

Below are the results of magnetic measurements on the magnetic samples. In the plots 'reference' refers to an as-received sample (Table 3.1).

3.2.2.1 LowDy Magnets in Argon

Figure 3.2 contains pictures of the magnet covered in 5 µm Dy at various points of the annealing process. As more annealing cycles were conducted, some samples, most notably the 5 µm sample, developed a dark-blue hue. The blue-color was most evident in the sample after 2 hours of annealing, and became more of a grey color during subsequent annealing rounds. When looking at the bottom of the sample, color changes appear to have been focused around the edges.

t_{Dy} = 5µm	1 hour	2 hours	4 hours
Bottom			
Top			

Figure 3.2. Images of magnets with 5 µm coatings after HT annealing for 1, 2, and 4 hours.

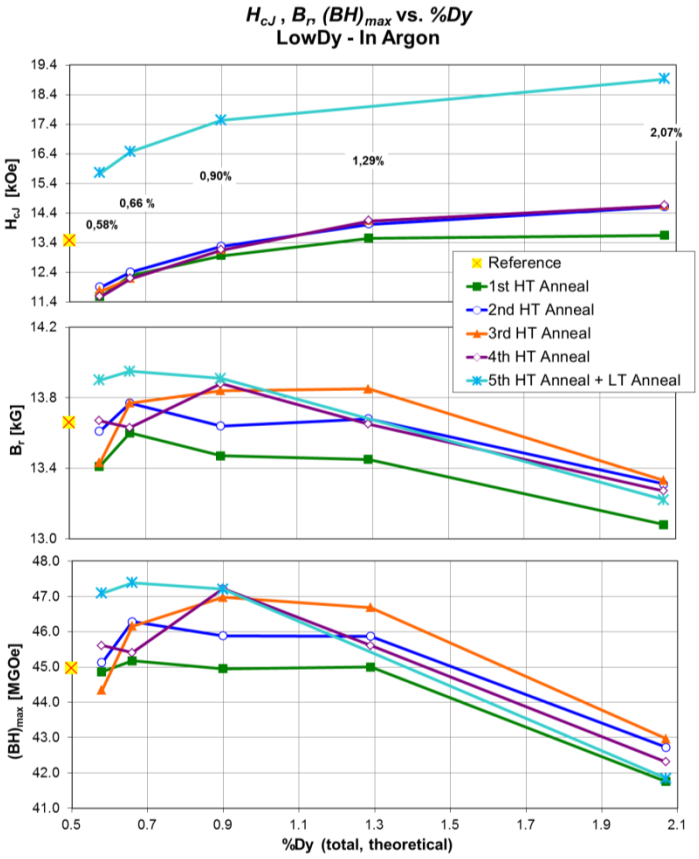

Figure 3.3. Change in H_{cJ}, B_r and $(BH)_{max}$ with *%Dy* and annealing time for the lowDy magnets in argon.

Figure 3.3 presents H_{cJ}, B_r and $(BH)_{max}$ of the lowDy magnets with respect to annealing time and Dy inclusion. A reference sample was not annealed in this trial. H_{cJ} of the coated magnets increased with Dy addition, becoming especially pronounced after the LT annealing. Values of B_r increased, but stayed relatively close to the reference value when Dy contents of under about 1,29% were present. B_r generally increased with annealing time until the fourth HT annealing. After low temperature annealing, B_r increased or remained constant for Dy inclusions of 0,90% and below. Almost all samples, to the

greatest extent the samples annealed at HT for 4 hours, show a $(BH)_{max}$ higher than the original samples until a Dy inclusion of about 0,90%. The form of the graph looks similar to the plot of B_r.

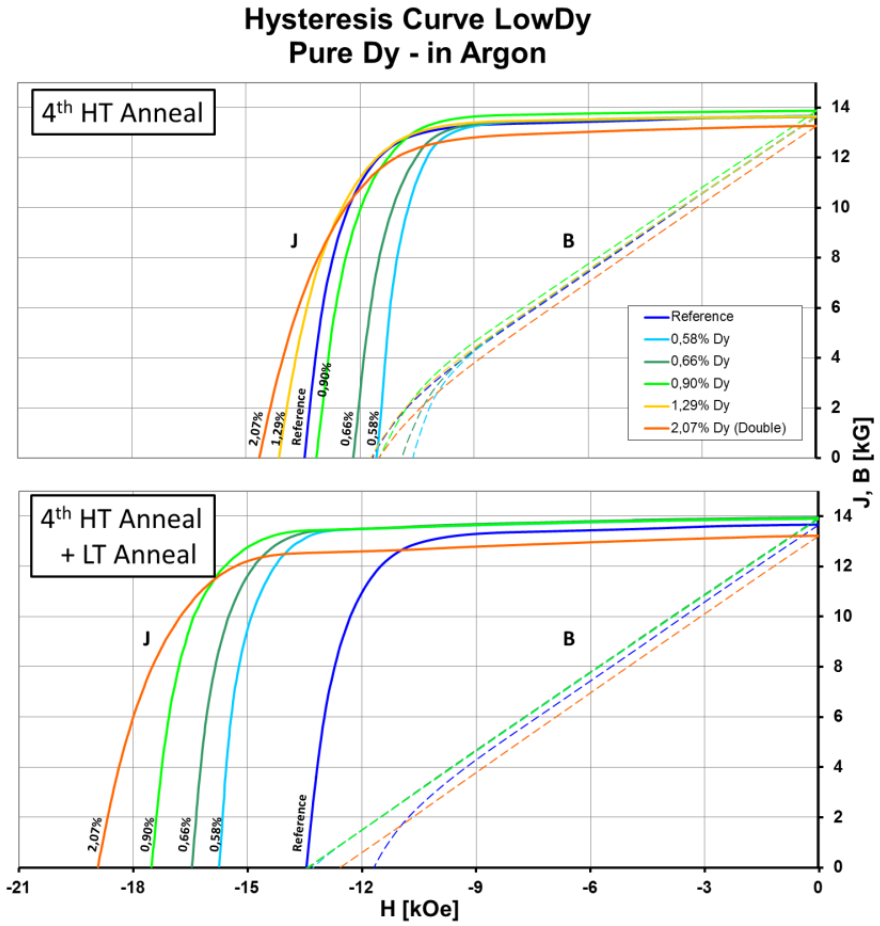

Figure 3.4. Demagnetization curves for the lowDy samples in argon.

Upon viewing Figure 3.4 and H_{cJ} in Figure 3.3, the significance of the low temperature annealing becomes apparent. In both of the hysteresis curves, the sample coated with 20 µm Dy, indicating a total of 2,07% Dy shows a lower B_r and a less square-shaped curve. When comparing the curves before and after LT annealing, the shape of $J(H)$ does not change drastically; however, the $B(H)$ curve becomes noticeably straighter. The knees present in the $B(H)$ curve are eliminated after the LT annealing. The 1,29% Dy sample was is not present in the LT annealing curve, as it was sent for SEM imaging before LT annealing occurred.

3.2.2.2 LowDy in Vacuum

Upon removing some of the samples from the Mo casing, some of the coatings adhered to the Mo, the thicker coatings to a greater extent (Figure 3.5). The adhesion was a larger concern for the magnets with higher coating thickness.

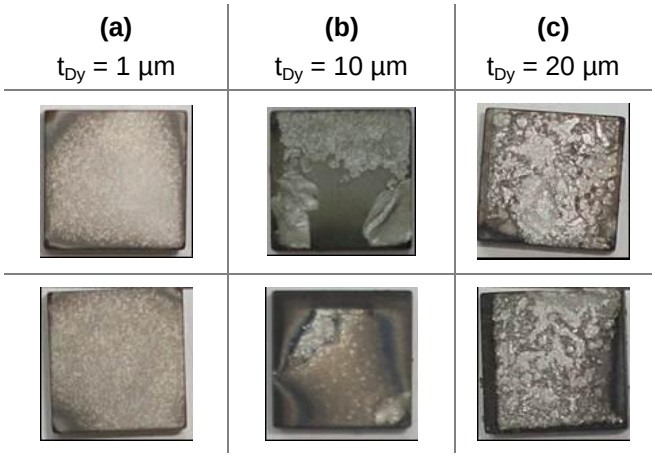

Figure 3.5. Images of the lowDy magnets coated in pure Dy after the first annealing cycle and being unwrapped from the Mo packaging.

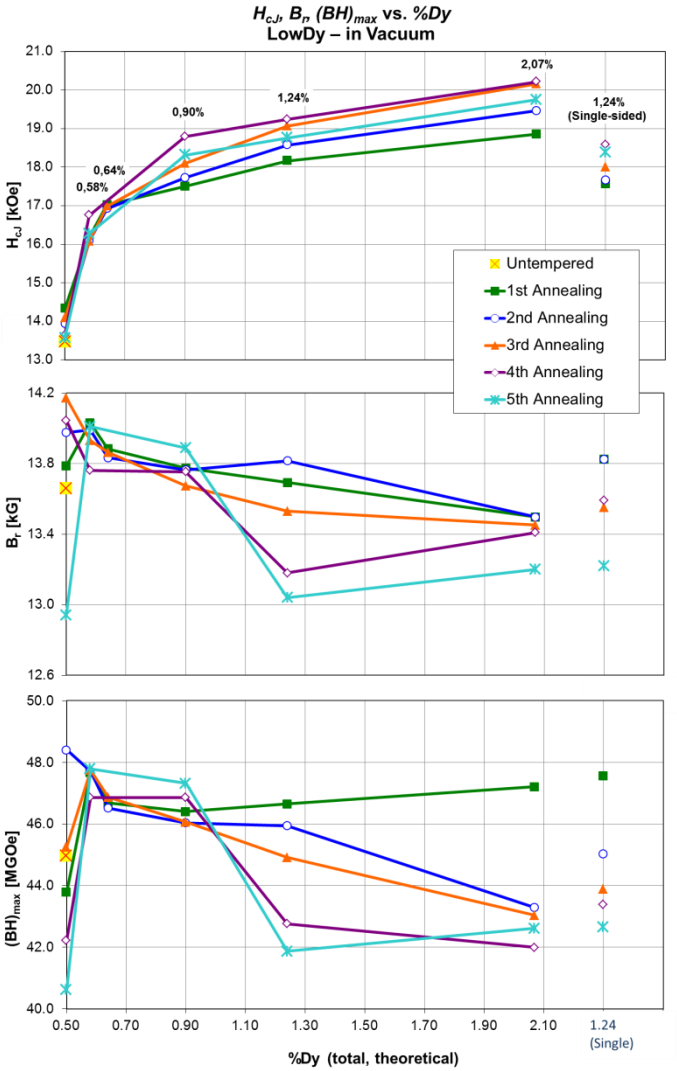

Figure 3.6. Change in H_{cJ}, B_r and $(BH)_{max}$ with *%Dy* and annealing time for the lowDy magnets in vacuum.

Figure 3.6 shows the change in H_{cJ}, B_r, and $(BH)_{max}$ with annealing time and Dy content. The first three annealing cycles were performed with one set of magnets, which had to be replaced for further testing due to a leak in the vacuum system, causing them to oxidize. The fourth and fifth set were then annealed for four and five hours straight, respectively, followed by an hour of low-temperature annealing. The coercivity was found to increase with Dy content and annealing time, although not in a linear fashion. B_r decreased with increasing wt% Dy and annealing time. However, it seems that the decreases became more prevalent after additions of about 1,24%Dy, when comparing the samples annealed for 1 hour and the samples annealed for 4 hours. As a general trend, including the magnets annealed in argon and the highDy series magnets, the losses in B_r seem minimal (or B_r increased) with low Dy-inclusion. The relative changes in the values of $(BH)_{max}$ follow the same trend as B_r, and does not increase with H_{cJ} enhancements. Small additions of Dy led to increases in $(BH)_{max}$, whereas anything over about 0,90% had an adverse effect.

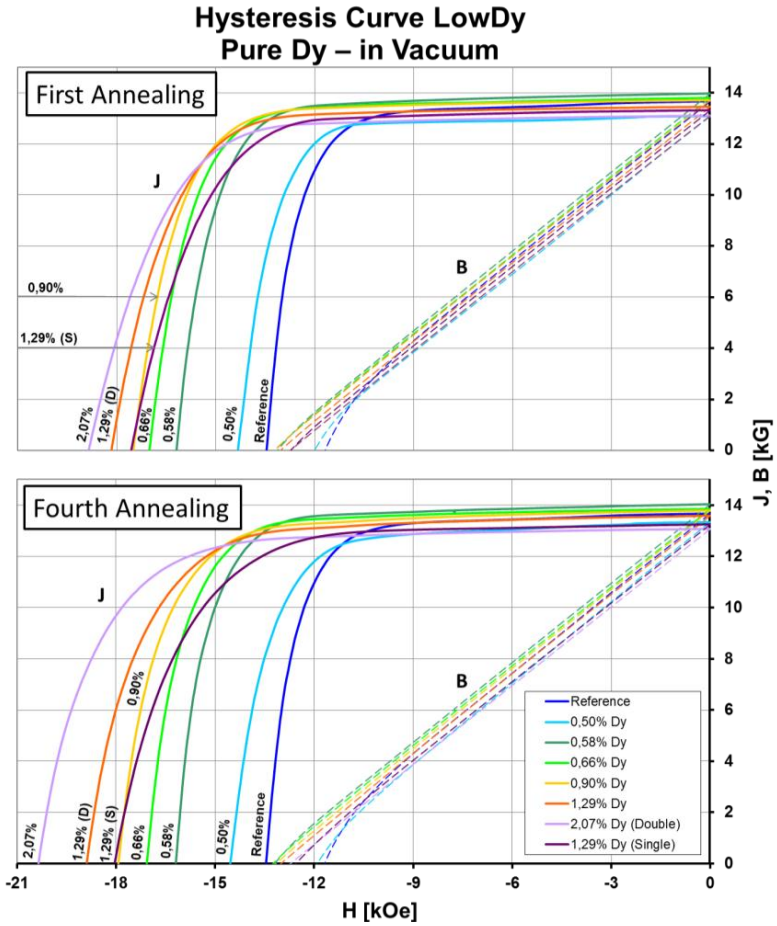

Figure 3.7. Demagnetization curves of the lowDy Dy-coated samples in vacuum.

Figure 3.7 shows the demagnetization curves for samples after one and four annealing cycles. Examining the hysteresis loop for the 1,29% Dy samples gives some insight into

the diffusion distance and inhomogeneous nature of the magnet compositions once diffusion has occurred. From these curves one can see the loss of squareness as well as decrease in H_{cJ} in the 1,29%Dy sample coated only on one side.

3.2.2.3 HighDy Magnets in Vacuum

Figure 3.8 shows the coatings of the highDy samples after being annealed at 900 °C for 4 hours. Coating damage seems to be minimal, and less of the magnet itself was torn off during packet separation. However, the surface damage (as seen previously) was more pronounced for higher amounts of Dy present.

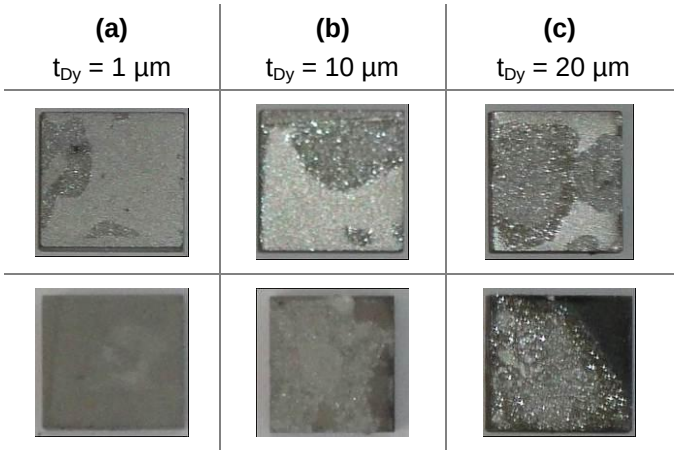

Figure 3.8. Images of the highDy magnets coated in pure Dy after 4 annealing cycles, followed by removal from the Mo packaging.

In the following figures, all of the samples are double-sided with the exception of the sample with 5,22% Dy in the third annealing stage, for which a magnet with 20 µm Dy on a single side was used. Figure 3.9 shows the changes in in H_{cJ}, B_r, and $(BH)_{max}$ for the various annealing times of the highDy magnets. Values of H_{cJ} for the single-sided sample were lower than the double-sided sample, and relative gains in coercivity were more pronounced when coating thicknesses were low (closer to the reference/uncoated sample). B_r values were higher for the magnets coated on a single-side and appear to be about level until reaching 4,65% Dy, after which values fell. Also, after the fourth annealing B_r of the uncoated sample dropped substantially.

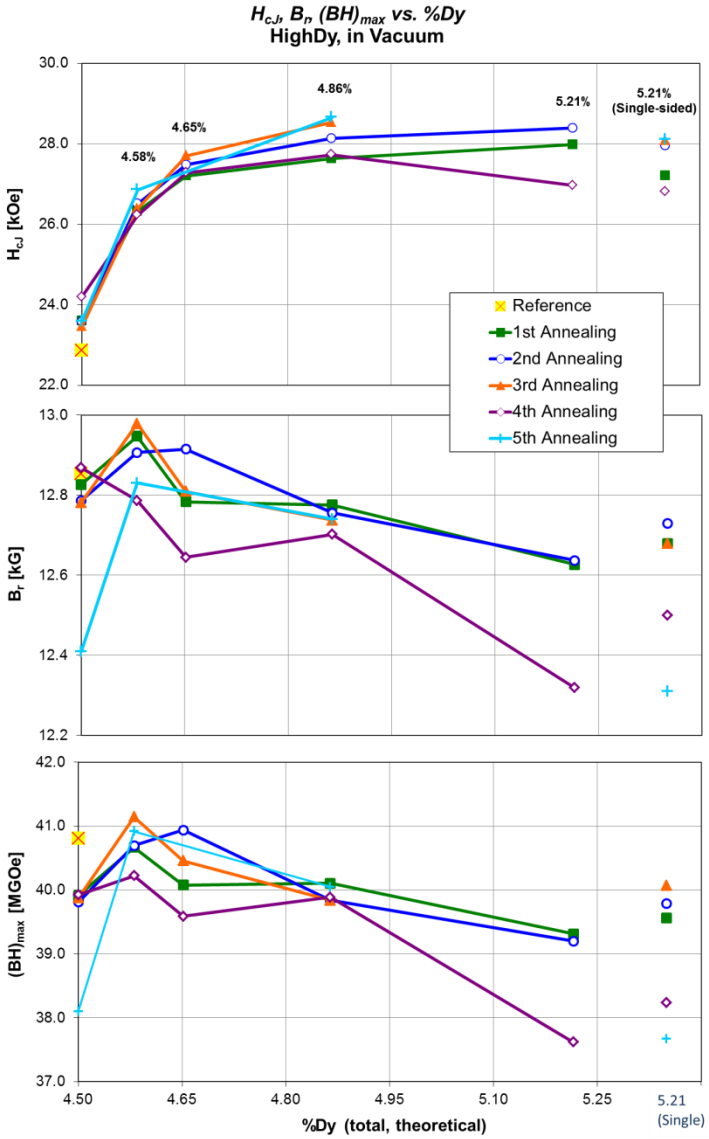

Figure 3.9. Change in H_{cJ}, B_r and $(BH)_{max}$ with *%Dy* and annealing time for the highDy magnets in vacuum.

Figure 3.10 shows the demagnetization curves for the highDy samples after one and four annealing cycles. Changes in the curve are not very pronounced, especially in comparison to the lowDy samples, and the induction curves are all straight. In the fourth annealing, in which samples underwent a four hours straight of HT annealing followed by 1 hour of LT annealing, coercive values for samples with higher Dy-contents (4,86% and 5,21% Dy) were lower than at the end of three complete annealing cycles (HT and LT annealings in 1 hour intervals). Magnets with lower Dy-contents showed improved or similar values.

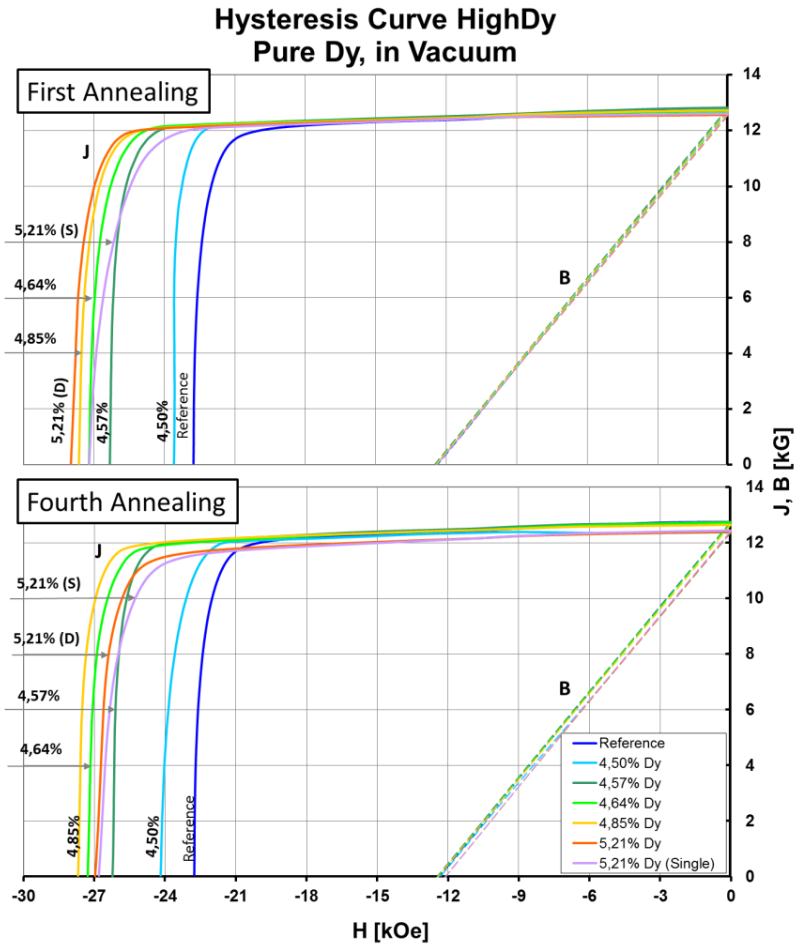

Figure 3.10. Demagnetization curves for the highDy Dy-coated samples in vacuum.

3.2.3 Microstructural Analysis

3.2.3.1 LowDy Samples

The SEM figures shown in Figure 3.11 display the depth profile of a lowDy magnet coated with 10 µm of Dy and annealed at 900 °C for 4 hours. The bright white areas are indicative of Nd-rich regions, light grey areas contain dysprosium (assumed to be the (Dy, Nd)$_2$Fe$_{14}$B phase), and the darker grey areas are the hard magnetic phase. Another feature of the SEM images is the refinement of the Nd-rich pockets at the grain junctions. The depletion of Dy as when approaching the inner-region of the magnet, first within the grain and then in the grain boundaries is also evident.

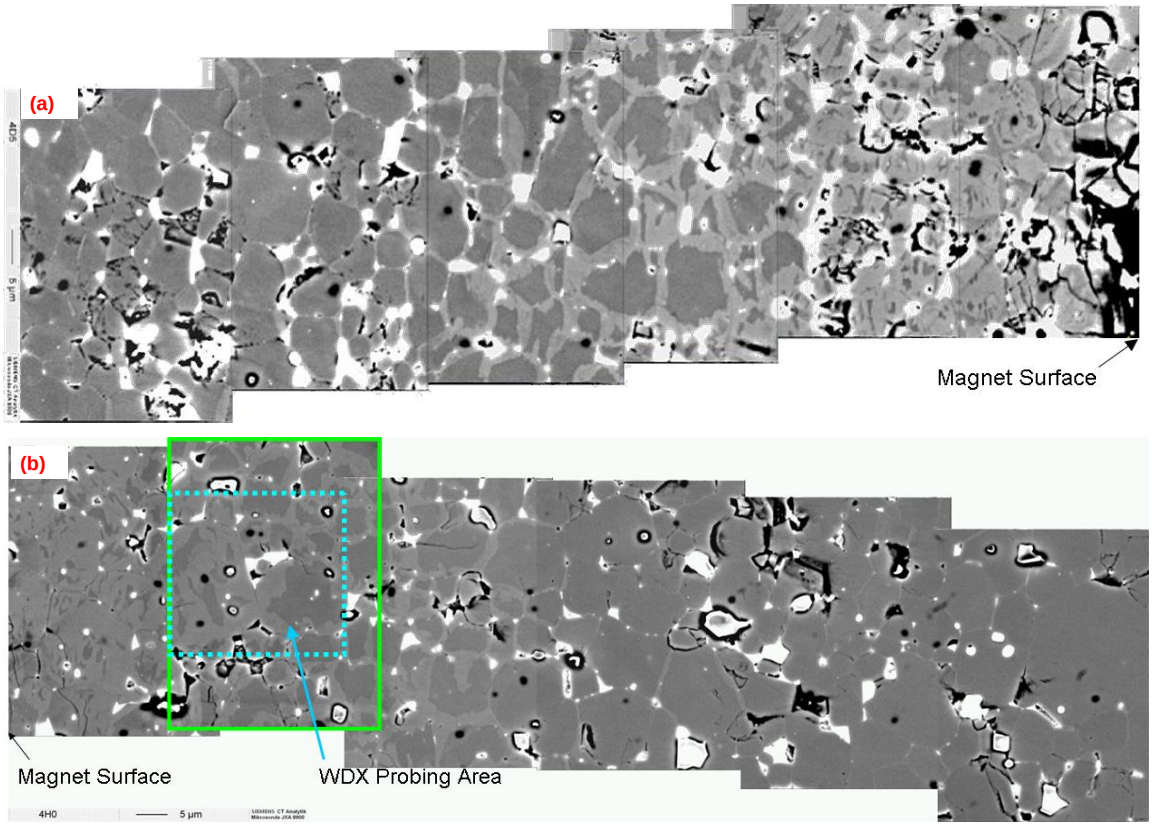

Figure 3.11. BSE images of the magnetic profile, using EPMA elemental-sensitive imaging of a lowDy magnet coated with 10 µm of Dy and annealed for 4 hours. Coating begins on the right side in (a) and the left side in (b).

The areas closer to the surface appear to have a high density of cracks and damage, as well as a higher Dy content. Figure 3.12 presents EPMA elemental analysis and WDX maps of the lowDy magnets. The Dy-rich borders, as well as the concentration in the magnetic grains and the Nd-rich pockets, area easily seen.

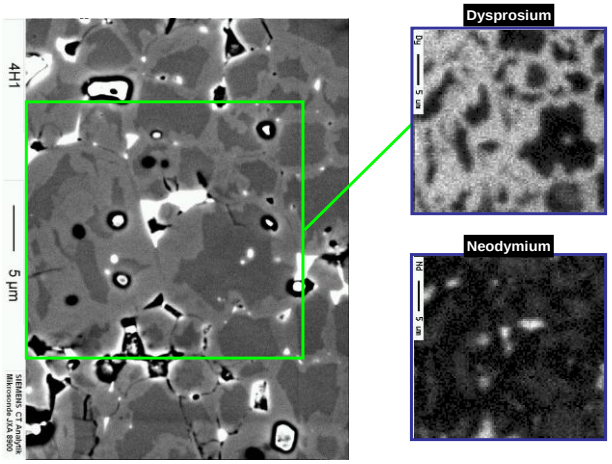

Figure 3.12. EPMA Elemental analysis and WDX maps of lowDy magnet coated with 10 µm of Dy and annealed for 4 hours.

Figure 3.13 shows BSE and WDX analysis of the lowDy magnets after 4 hours of high-temperature annealing. Near the grain boundaries, there are areas where the image appears a lighter grey in Figures 3.11 and 3.12. The WDX images affirm that these are areas in which Dy has collected. The grains interiors are also seen to consist of Nd, Fe, and to some extent Co. Grains with Dy as the predominant rare earth (RE) present were not seen: Dy was largely confined to the grain boundary and periphery. Nd-rich regions and areas rich in Nd and Fe are also seen; however, the Nd along the grain boundaries appears to be less abundant than in the magnetic grains. RE rich areas exist at the grain junctions and grain boundaries. Iron is well dispersed throughout the system, with the exception of the RE pockets.

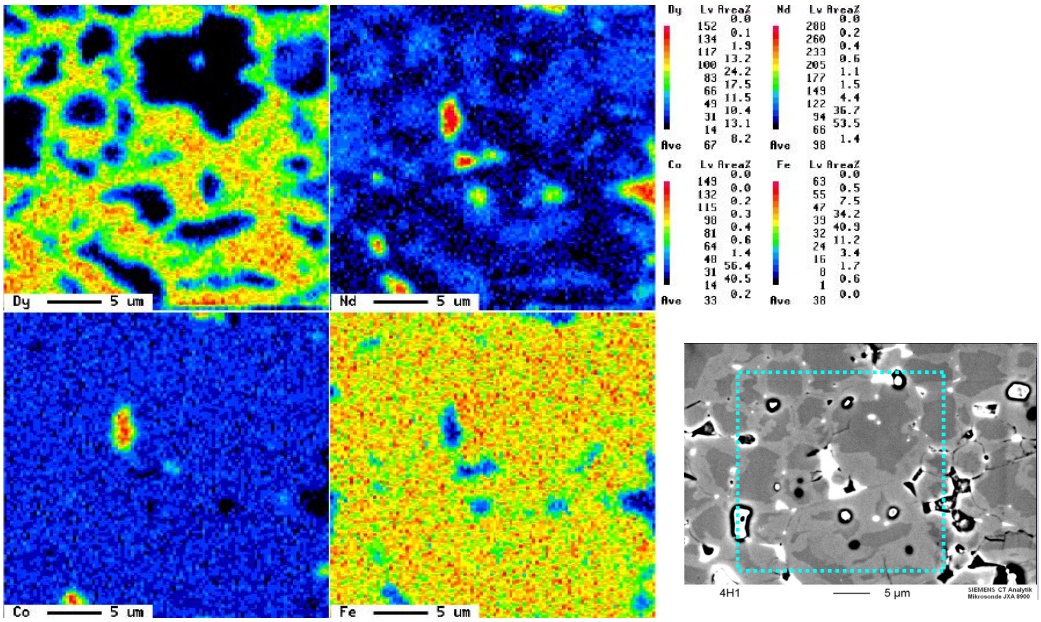

Figure 3.13. BSE and WDX imaging of the lowDy magnet.

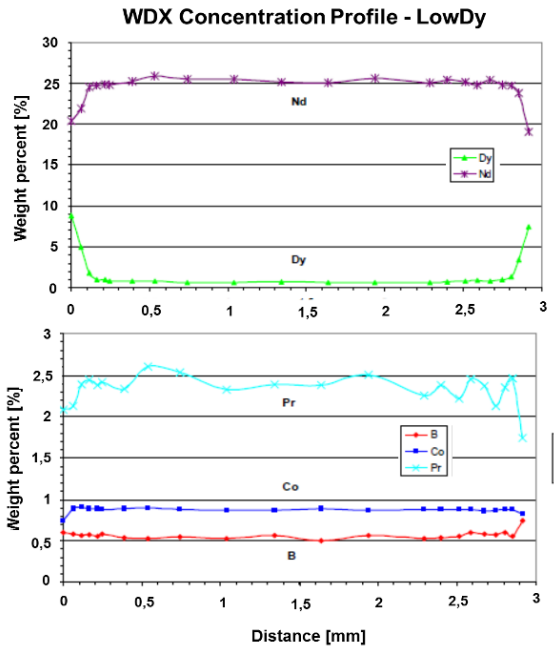

Figure 3.14. WDX depth profiles for Nd, Dy, Pr, Co and B in the lowDy magnet.

The total depth to which the Dy diffused was about 100 µm, as seen in the WDX concentration profiles (Figure 3.14). These curves illustrate the reduction of Nd, Pr and to some extent Co near the magnet surfaces. In this region, the amount of Dy reaches a maximum of about 9% at the sample surface. At this point a minimum of Nd (at about 20%), Co, and Pr are also seen. The amount of rare earths in the structure remains relatively even, totaling about 29-30%. This reduction of the Nd-phase near the surface may also be correlated to the lowered amount of Nd in the grain boundary phase seen in the WDX images.

3.2.3.2 HighDy Samples

Figure 3.15 presents BSE images of the highDy magnets, profiling the depth of the samples. Dy is present around the grains to a distance of about 100 µm below the surface. The area near the surface also displays many pores, cracks, and gaping grain boundaries. Rare-earth rich areas are seen at the grain junctions and grain boundaries, as witnessed by the bright patches. Compared to the lowDy samples, there is much less grey contrast in the area of the grain boundary.

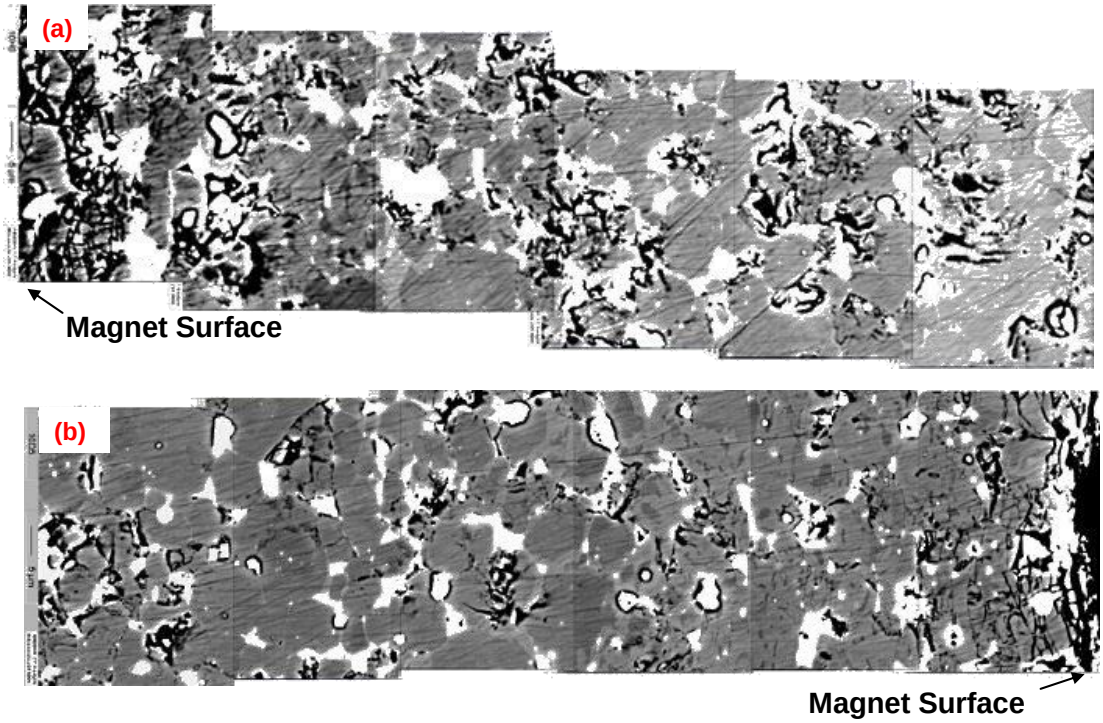

Figure 3.15. BSE images of the highDy magnet after four annealing cycles with the surface of the magnet at the (a) left and (b) right side.

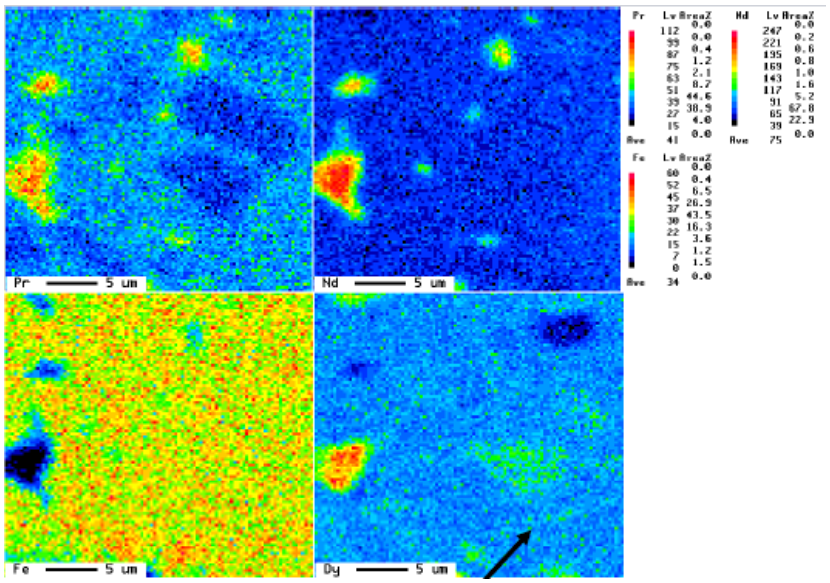

Figure 3.16. WDX Elemental mapping of the highDy sample coated with 10 µm Dy and annealed for four cycles.

Figure 3.16 Shows the WDX compositional imaging of the highDy sample. The Dy-enriched grain boundaries are still visible, although to a lesser extent than the lowDy samples. Grains rich in Pr, Nd, and Dy are observed. The arrow in the Dy-image indicated an area which is expected to be a grain boundary.

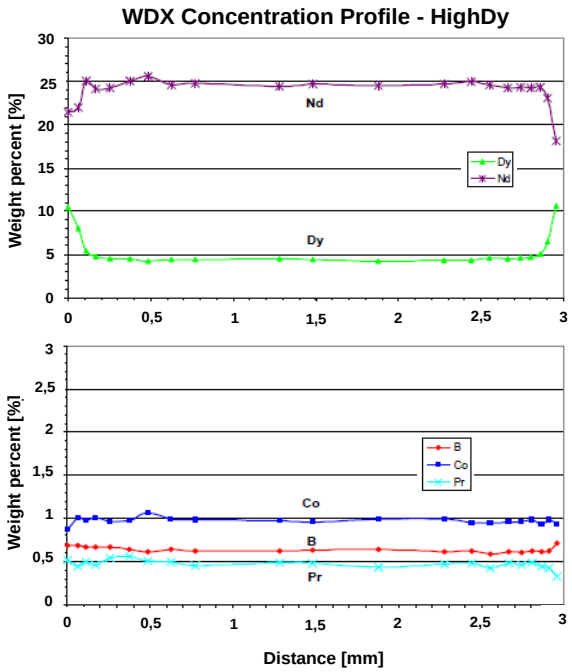

Figure 3.17. WDX concentration profile for Nd, Dy, Pr, Co and B in the highDy samples.

Figure 3.17 shows WDX concentration profiles of Nd, Dy, Co, B, and Pr. There is a noticeable increase in Dy at the edges, with a maximum of about 10,5% Dy, which is accompanied by a decrease in Nd content, with a minimum at about 18-21% Nd. The Dy is seen to diffuse into the sample to a depth of about 100 µm, after which point it levels out at the original Dy content of about 4,5%. The amount of rare earths present at any point in the magnet is almost constant, totaling about 31%.

3.3 Dy-Cu Coated Samples

3.3.1 LowDy Magnets with Dy-Cu Coatings

Figure 3.18. shows images of the magnets coated with Dy and Cu after annealing for one cycle (1 hour at 900 °C + 1 hour at 500 °C). The magnets with higher Cu contents were much more difficult to remove from the casing compared to the pure Dy coated magnets.

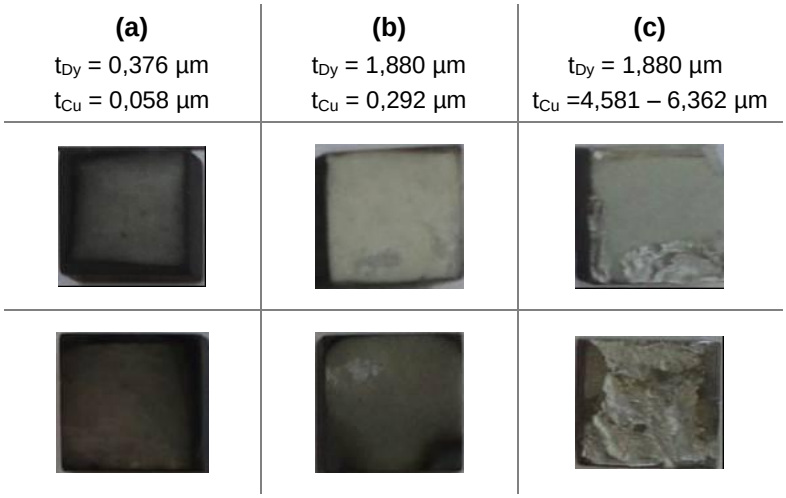

Figure 3.18. Images of the lowDy magnets with Dy-Cu coating after one annealing cycle.

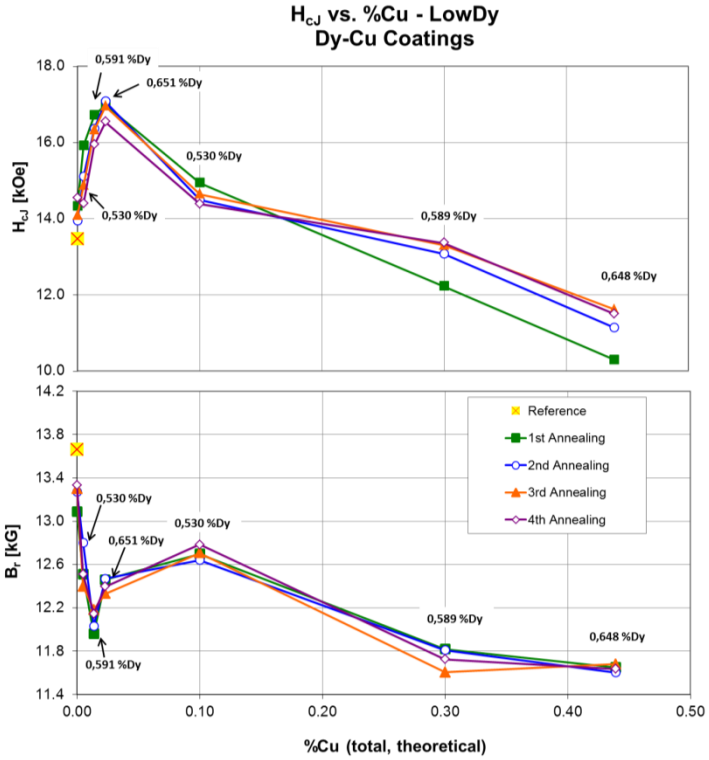

Figure 3.19. Change in H_{cJ} and B_r with increasing Cu content for the lowDy samples. Corresponding Dy-contents are indicated.

Figure 3.19 shows the relative effect of additional Cu on H_{cJ} in the Dy-Cu system. There does appear to be an increase in H_{cJ} at low additions of Cu. The additions of Cu also had

a negative effect on B_r. It is important to note that the increase seen at 0,10% Cu in the plot of B_r in Figure 3.19 is also a point where less Dy is included in the magnet, relative to the two previous samples.

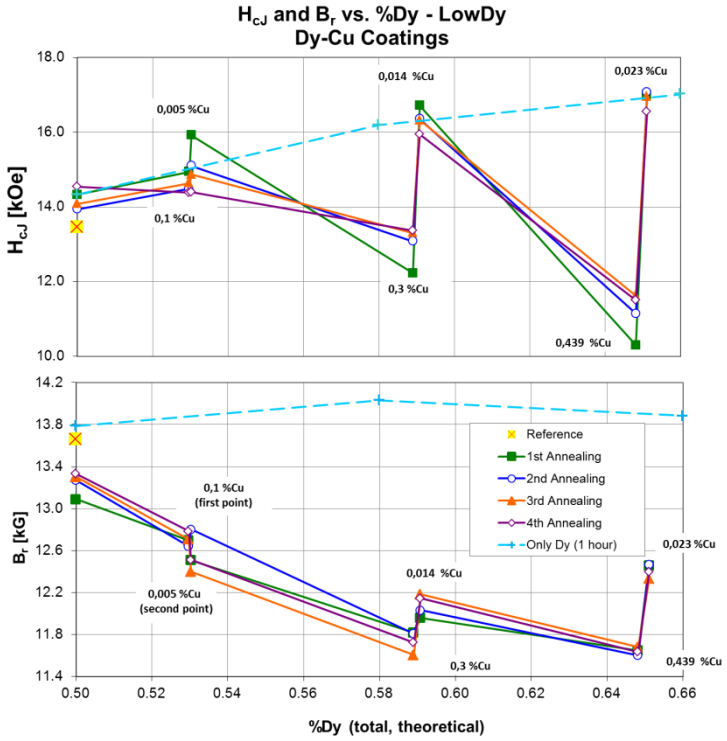

Figure 3.20. Change in H_{cJ} and B_r with increasing Dy content for the lowDy samples, as compared to a magnet coated only in Dy. Corresponding Cu-contents are indicated.

Figure 3.20 affirms the observation that higher Cu contents have an adverse effect on the coercivity, as seen by the drops in coercivity for samples with almost the same amount of Dy and differing Cu contents. Improvements to the coercivity compared to the samples without Cu are seen only in samples with very little Cu and annealed for very short times. Improvements in B_r are not seen for any values.

Figure 3.21 shows the effect of increased Cu inclusion on the shape of the demagnetization curves after the first and fourth annealing cycles. The magnetic properties of the samples with high Cu-contents were compromised, showing a reduction in squareness, B_r and H_{cJ}, as well as enlarged knees in the induction curves

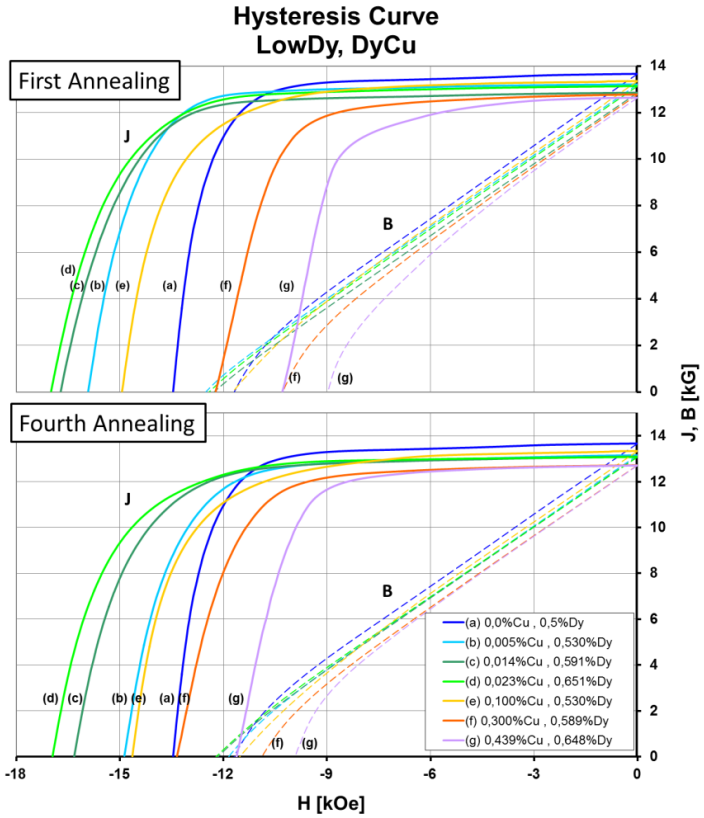

Figure 3.21. Demagnetization curves for the lowDy Dy-Cu-coated samples.

3.3.2 HighDy Magnets with Dy-Cu Coatings

Seen in Figure 3.22 are some images of the Dy-Cu coated magnets after being removed from the packaging. Coating damage, if it occurred, was similar to the lowDy samples.

(a)	**(b)**	**(c)**
t_{Dy} = 0,376 µm t_{Cu} = 0,058 µm	t_{Dy} = 1,880 µm t_{Cu} = 0,292 µm	t_{Dy} = 1,880 µm t_{Cu} =4,581 – 6,362 µm
		
		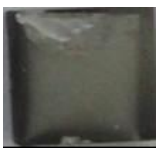

Figure 3.22. Images of the highDy magnets coated with Dy and Cu after one annealing cycle.

Figure 3.23 shows the effect of increasing Cu and Cu-content on H_{cJ} and B_r. The additions of Cu also had a negative effect on B_r, The increase at 0,10% Cu in Figure 3.23 is also a

point where less Dy is included in the magnet. The values appear relatively scattered; however, a consistent decrease in B_r with the number of annealing cycles is seen.

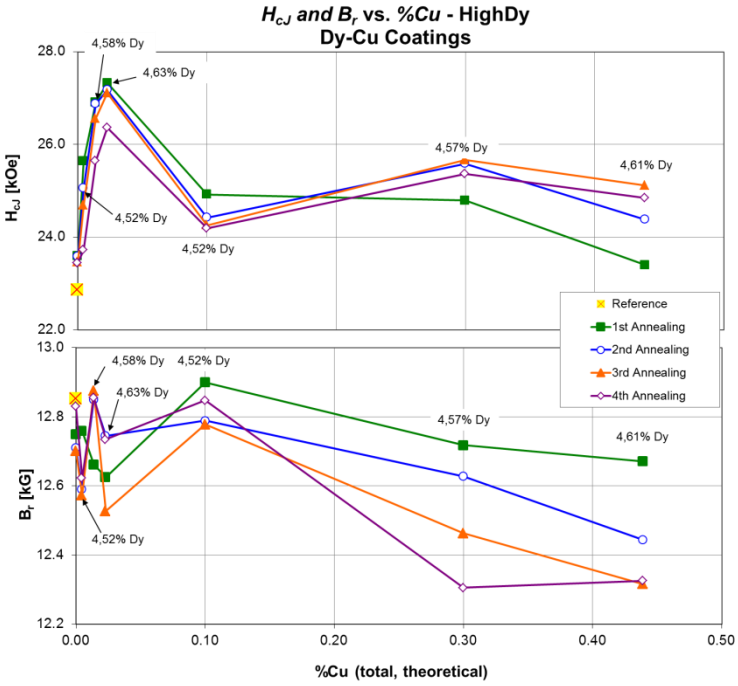

Figure 3.23. Change in H_{cJ} and B_r with increasing Cu content for the highDy samples, as compared to a magnet coated only in Dy. Corresponding Dy-contents are indicated.

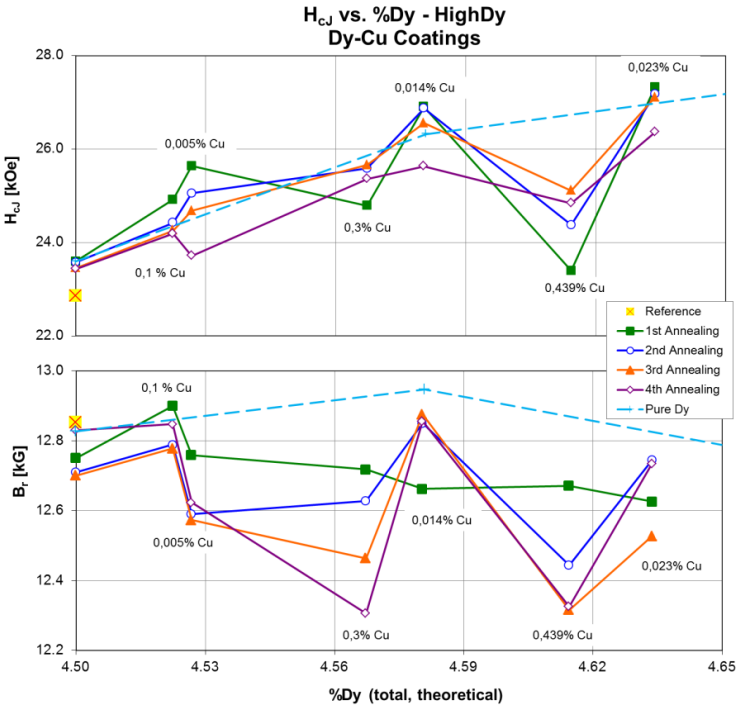

Figure 3.24. Change in H_{cJ} and B_r with increasing Dy content for the highDy samples, as compared to a magnet coated only in Dy. Corresponding Cu-contents are indicated.

Figure 3.24 shows the effect of increasing Dy content on H_{cJ} and B_r. It is clear that H_{cJ} and B_r generally decrease with consecutive annealing cycles, showing some improvement with respect to the uncoated, non-annealed samples for the initial annealings with low Cu-contents.

Figure 3.25 shows the demagnetization curves for the HighDy samples coated with various amounts of Cu and Dy after one and four annealing cycles. Changes in the hysteresis curves are much less pronounced than in the lowDy samples. The coercivity of the samples with lower Dy inclusion and higher Cu contents tend to decrease with annealing time, whereas the reverse is true for samples with higher amounts of Dy and lower amounts of Cu.

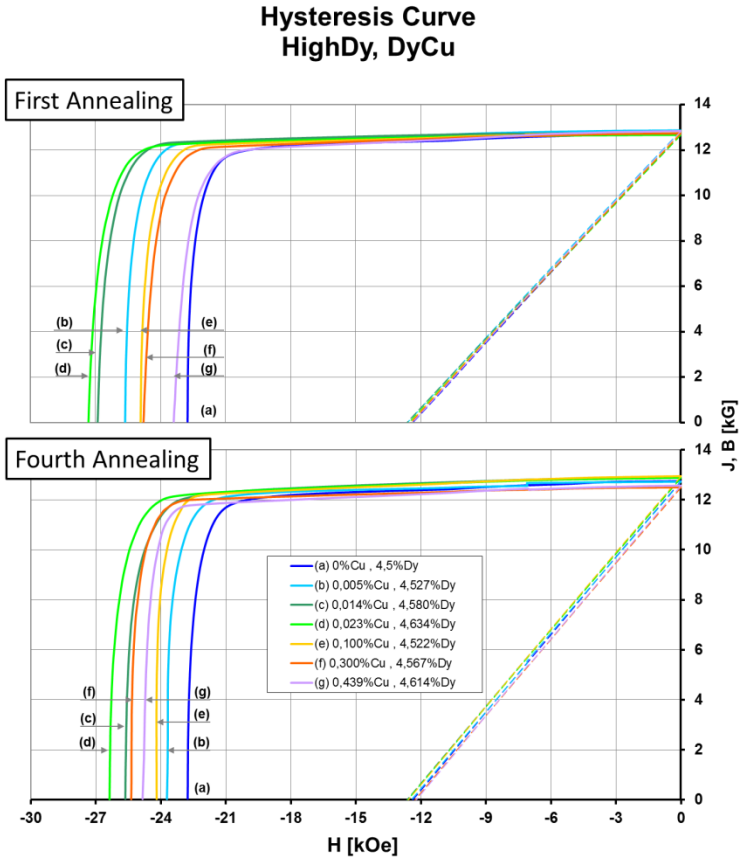

Figure 3.25. Demagnetization curves for the lowDy Dy-Cu-coated samples.

Chapter 4 - Discussion

4.1 Pure Dy Coatings

4.1.1 Coating Changes

The darkening of the magnets during annealing in argon (seen in Figure 3.2) is believed to be due to the diffusion of Nd (and possibly Dy) out of the bulk magnet or the coating, which would have then released into the annealing environment and (re)deposited onto the magnet surface. This may explain the thick, black crust formed on the samples coated with 10 µm and 20 µm of Dy when the samples were annealing in argon, and is believed to be confirmed by the blackening of non-coated magnets in areas where diffusion of the leached Nd or Dy was hindered, for example where the magnet was very close to the quartz tube. Additionally, some black residue was noticeable on the quartz tube of the oven, which was only partially removed after a KOH bath. Black surfaces have also been reported in oxidation studies of NdFeB magnets, so it is also possible that the vacuum system was compromised at some point, although this would have most likely also led to the properties of the magnet worsening as annealing cycles progressed. The blue-ish hue seen in the samples annealed in argon could be attributed to the cobalt in the sample at the surface, for example if the cobalt from the magnet reacted with silicate somehow from the quartz tube to form cobalt silicate. This may be the reason that blue hues were not observed in the magnets annealed in Mo casing.

The encasing in molybdenum was thought to reduce or eliminate the occurrence of Nd diffusing out of the magnet; however, this system sometimes resulted in parts of the coating and the bulk chipping off while the magnets were being unpacked. After annealing cycles in which any part of the coating or magnet was removed, the magnets were reweighted and the Archimedes principle was used to determine the new sample volume, which could then be used to calculate a more reliable value for the remanence.

4.1.2 Coercivity

The coercivity is expected to increase proportionally to the amount of Dy substituting Nd in the $(Nd, Dy)_2Fe_{14}B$ phase. The results of increases in the coercivity after a given time would then indicate that the interdiffusion of Dy into the magnetic structure does not occur on a linear time scale. This is supported by the group of Popov, et al[12], which found that after the first hour of annealing the diffusion mechanism switched of Dy switched from grain boundary diffusion to bulk diffusion. The shape of the $\boldsymbol{H_{cJ}}$ curve is of a similar form.

Grain boundary diffusion is very complex. The substitution of Dy into the $Nd_2Fe_{14}B$ grain relies not only on the incorporation of Dy into the grain, but also the exodus of Nd out of

the grain to the boundary. As more Dy is substituted into the grain, both the entering Dy and the rejected Nd must travel farther before interdiffusion can be completed, so a reduction in $\boldsymbol{H_{cJ}}$ gains relative to time would be expected. However, the expelled Nd atoms also serve to enrich the low melting-temperature Nd- rich GB phase, improving the properties of the network through which Dy travels and increasing the possible diffusion depth of the Dy atoms into the sample. To complicate this, at intermediate temperatures one would have to consider the presence of both solid and liquid grain boundaries, for which the relative diffusivities would vary. The reduction in Nd in the grain boundaries seen in WDX images would hint that perhaps the expelled Nd from the magnetic grains is collected at grain junctions and/or removed from the magnet at areas near the surface, rather than serving to enrich the grain boundary.

It is also possible that gains in the coercivity were reduced due to oxidation of the sample, especially at the corners which rested upon the quartz tube. Nd is slightly more electronegative than Dy, and both are more electronegative than Si (χ^A_{Nd} = 1,07 - χ^A_{Dy} = 1,10 - χ^A_{Si} = 1,74, Allred and Rochow)[5], which means that the corners resting on the quartz may have reacted with the oxygen from the quartz tube. This was also apparent from the formation of small etching marks in the tube after the annealing in argon. These etchings were more prevalent in samples with thicker Dy coatings. This may also explain the darkening of the quartz tube, which may have been due to Nd or Dy diffusing out of the magnet and reacting with the environment. It was because of these concerns that the samples were later annealed in the Mo casing. However, the reduction in Nd present near the edges in both the samples annealed in argon and those in the Mo casing suggests that the amount of Nd diffusing into the furnace during annealing was minimal. Additionally, even when the casing was used there were times when the vacuum of the annealing environment was compromised. The Mo casing may also have hindered the amount of Dy being incorporated into the magnets because of the adherence of the coating to the Mo casing.

Overlaying the remanence curves of the lowDy and highDy samples (after 3 annealing cycles) yields Figure 4.1. In this plot, the relative effect of GBD in comparison to Dy introduced during the annealing process can be easily seen. The line representing magnets with NdFeB inclusions during sintering is an extrapolation of the reference sample data. A best fit line was considered suitable because of reports by Suzuki[13] and Herbst[35] indicating a linear relation of $\boldsymbol{H_{cJ}}$ and Dy-inclusions, as well as the intercept near 12 kOe, which matches the value reported by Li[9] for NdFeB magnets without Dy additions. At higher inclusions, GBD is no longer a suitable measure as the coercivity

plateaus for increasing amounts of Dy. The most important implication of this is the understanding that for small Dy additions to the NdFeB systems, the gains made with GBD are more pronounced than those through increasing the Dy inclusions during sintering.

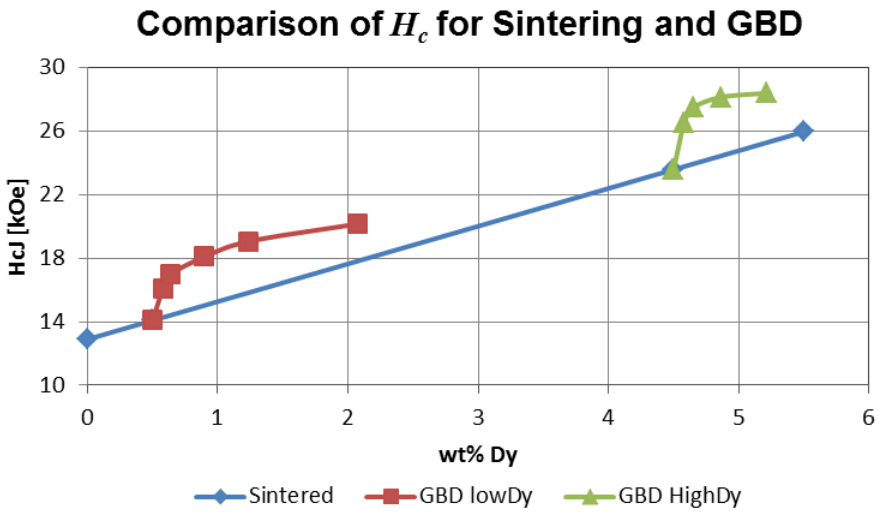

Figure 4.1. Comparison of Dy inclusion during the sintering process and as part of GBD.

However, there are misunderstandings which may arise from Figure 4.1, and it is important to also consider the microstructure and Dy dispersion within the sample. Because the Dy coating is concentrated within the first 100 µm of the sample, the coercivity values reported most likely reflect the coercivity in this region, where the %Dy was around 10%, rather than the bulk. The %Dy reported reflects an average throughout the sample, so the slope of the H_{cJ} increases made through the GBD process with increasing %Dy may be more like that seen in the beginning of the GBD curves.

Assuming the shape, size, initial composition, etc. is the same as the samples from the current works, the values collected may be considered valid; however, these results may not be extrapolated to samples with other characteristics. Comparing these results to those previously reported, assuming all of the Dy near the surface interdiffuses (totaling a 10% substitution), the values for the coercivity are still lower than the theoretical 30 kOe suggested by Oono[18] for this amount of substitution. This may be because of defects (such as the cracking also witnessed near the surface) serving as sites for reverse domain nucleation. This is a good insight as to why more Dy is alloyed in typical applications; some safety factor for the coercivity is needed to ensure that produced magnets reliably function under the operational conditions.

4.1.3 Remanence

The marked reduction in $\boldsymbol{B_r}$ witnessed at higher Dy inclusion, most notably 1,24% Dy in the lowDy samples and 4,86% for the highDy samples annealed in Mo casing, was expected. However, any increases from the reference sample, as seen in some of the samples with lower Dy-inclusions, would not have been expected. The increase with small additions of Dy may be due to the properties of the original magnets varying to some extent, or inconsistencies in the magnetic measurement device. Because of the higher rare-earth inclusion in the highDy magnets (about 31% in the highDy magnet and about 29% in the lowDy magnets, the presence of Pr serves to mediate the discrepancy in RE between the two samples) and the higher Fe-inclusion in the lowDy magnets (about 68% in the highDy magnet and about 70% in the lowDy magnets) coupled with the stoichiometric restrains of the hard magnetic phase, it would be expected that the magnets with higher Fe contents would be able to form a larger volume fraction of hard magnetic phase. These RE and Fe proportions as well as the antiparallel coupling of Dy to Fe in the hard magnetic phase could be reasons for the higher $\boldsymbol{B_r}$ values seen in the lowDy magnets.

The decreases in remanence may also be due to the localized concentration of diffused Dy near the surface. Because $\boldsymbol{B_r}$ is a bulk property of the sample, even if a large decrease in $\boldsymbol{B_r}$ occurs, the small volume it influences is effectively compensated by the bulk of the sample.

4.1.4 Maximum Energy Product

At some point, gains in $\boldsymbol{H_{cJ}}$ no longer affect the intercept of the induction curve ($\boldsymbol{B(H)}$, $\boldsymbol{H_{cB}}$). Because the $\boldsymbol{B(H)}$ curve which is used to determine $(BH)_{max}$, only increases in $\boldsymbol{B_r}$ will lead to an increased maximum energy product. This explains similarities in the $\boldsymbol{B_r}$ and $(BH)_{max}$ curves when considering the shapes of the curves, as well as why the reference magnet with 0,5 wt% Dy has a higher value of $(BH)_{max}$. The energy product only saw improvements in the magnets with low Dy-contents, up to about 0,9% Dy, showing values of about 46-48 MGOe. However, as with $\boldsymbol{H_{cJ}}$ and $\boldsymbol{B_r}$, the small diffusion distance of Dy into the samples makes application of the values collected in this experiment to others difficult.

4.1.1 High and Low-temperature Annealing

The second annealing of the samples at lower temperatures results in an increase in the $\boldsymbol{H_{cJ}}$, and in most cases $\boldsymbol{B_r}$ as well. The annealing at low temperatures may reduce stresses induced by the rapid cooling of the sample from the high temperature. It may also aid in the recovery of defects which otherwise may serve as nucleation sites for reverse

domains or the formation of a more continuous, non-magnetic intergranular phase to increase magnetic grain decoupling. As witnessed in the samples annealed in argon (Figures 3.3 and Figure 3.4), the low temperature annealing not only affected $\boldsymbol{H_{cJ}}$, but also removed or decreased the knee seen in $\boldsymbol{H_{cB}}$, indicating that these magnets should be more stable across a range of temperatures and applied fields than those without the LT annealing. The increasing linearity and the increase in $\boldsymbol{H_{cB}}$ are indicators of more stable magnets.

4.1.1 Comparisons Between Tempering Series'

4.1.1.1 Argon vs. Vacuum

Compared to the samples annealed in argon, the samples in the Mo packaging and vacuum yielded higher values for $\boldsymbol{H_{cJ}}$ but lower values for $\boldsymbol{B_r}$. There are several possible explanations for this. First, the Nd leaving the surface of the magnet would most likely come from the Nd-rich phase. This would hinder the diffusion path of the Dy into the magnet by compromising the diffusion path. Another possibility is that the samples annealed in argon did not undergo LT annealing treatments in between HT annealing steps. This would effectively decrease the ability of the material to recover from HT annealing step by reducing stresses. It was shown by Vial, et al[25] that the LT annealing phase serves to refine the grain boundary, making the diffusion path for Dy more defined. The result of not performing LT annealing step may then have been a reduced degree of Dy diffusion through the grain boundary, and hence also into the magnetic grains. This hypothesis could also be related to the lower-than-expected coercivity from the lowDy samples in a vacuum after 4 hours of constant annealing. The samples were probably not oxidized, but were not as high as may have been expected based on an extrapolation of previous results. The total annealing time of samples annealed for 4 straight hours may also have been less than those that underwent multiple annealing cycles because the time needed for the sample to heat up and cool down would add to the total time in which diffusion could occur.

4.1.1.2 LowDy vs. HighDy

The initial values of $\boldsymbol{B_r}$ as well as observed reductions for the highDy samples were noticeably less than those of the lowDy magnets, as seen when comparing Figure 3.6 and Figure 3.9. Table 4.1 presents the changes in Dy for each coating thickness, as a percentage. A comparison of percentage change after one and three annealing cycles is shown in Figure 4.2a.

Table 4.1. Changes in Dy (%) for the various coating thicknesses, double-sided.

Thickness (µm)	lowDy		highDy	
	%Dy	%Δ Dy	%Dy	%Δ Dy
0	0,50	0,00	4,5	0
1	0,58	0,16	4,57	0,016
2	0,66	0,32	4,64	0,031
5	0,90	0,80	4,85	0,078
10	1,29	1,58	5,21	0,158
20	2,07	3,14	--	--

The relative (percentage) changes in H_{cJ} and B_r for the highDy magnets were about half those of the lowDy magnets when comparing the magnets with the same coating thicknesses, despite the highDy reference magnets (4,5% Dy) containing about nine times as much Dy as the lowDy reference magnets (0,5% Dy). This difference in gains or losses of H_{cJ} and B_r, respectively, may be expected because for an equal amount of coating being added to the magnet, the overall mass percentage of Dy changes is about 10 times less for the highDy magnets than the lowDy magnets. If this is taken into account, for every incremental %Dy added to the magnet, the highDy magnets actually had higher relative H_{cJ} increases and lower B_r losses (Figure 4.2b). This may be due to the interdiffusion of the Dy already present in the magnets, not only at the edge but also throughout the bulk. However, it must also be considered that only two data points were available to be used for the lowDy sample and the values for the lowDy and highDy samples containing the same relative increase in Dy have similar increases in H_{cJ}.

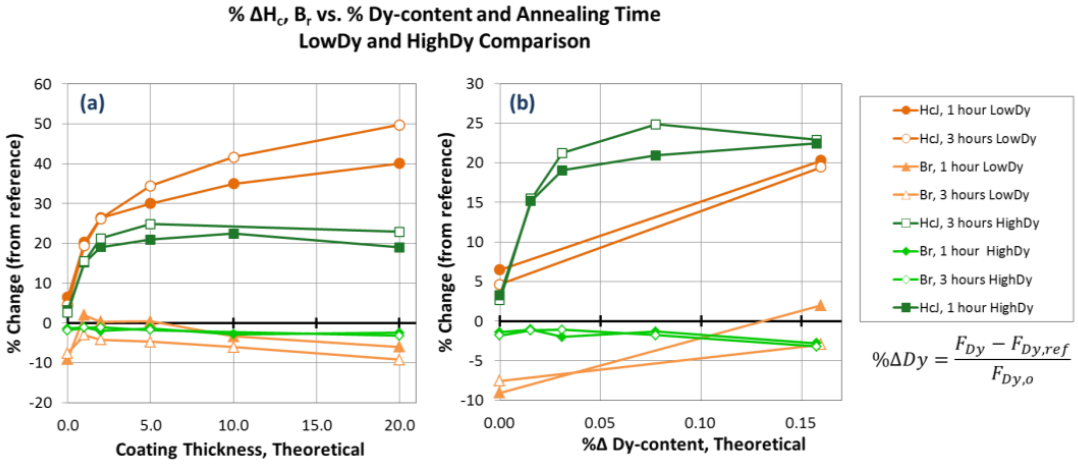

Figure 4.2. Comparison in % change of H_{cJ} and B_r for the lowDy and highDy samples, compared based on (a) coating thickness (µm) and (b) percent increase in Dy in the sample.

The relative (%) changes indicated in Figure 4.2 match well with those reported by Sepehri[10] and Soderžnik[38] (~50% increase) which underwent a similar heat treatment the those from this experiment. The absolute values for the initial and final coercivities also match well with those of the lowDy samples in this work with a total of 2,07 %Dy average.

Comparing the highDy hysteresis curves with those of the lowDy samples also shows that the gains in $\boldsymbol{H_{cJ}}$ are less pronounced in the highDy samples, which is logical given the higher initial amount in the samples. Unlike the lowDy samples, the shape of the highDy samples seems to be maintained, even at high coating thicknesses, although some loss of squareness is witnessed in the single-sided coated magnets, indicating a non-homogeneous structure.

The fourth annealing of the lowDy and highDy samples were performed simultaneously. It is unclear why $\boldsymbol{H_{cJ}}$ increases and the $\boldsymbol{B_r}$ of these samples decreases, whereas in the lowDy samples $\boldsymbol{H_{cJ}}$ increases and $\boldsymbol{B_r}$ remains about constant (except for at higher levels of Dy-inclusion). It is possible that the furnace was not able to be held under a vacuum during testing and some oxygen was incorporated into the magnets. It may also be that oxygen which was adsorbed onto the magnet or Mo casing surface reacted with the magnet during annealing.

4.1.2 Single vs. Double-sided Samples

The reduction in squareness of the hysteresis curve from the single-sided coatings of the lowDy sample (Figure 3.7), which became more pronounced as tempering proceeded, indicates that Dy was not able to disperse evenly throughout the sample. This is reaffirmed by the WDX images, which show a diffusion depth of around 100 µm for the Dy. Both double and single-sided samples would then contain inhomogeneous microstructures, as Dy is unable to diffuse throughout the entire magnet; however, the single-sided coatings would be even more inhomogeneous than double-sided samples. Because in many cases the rotation of domains originates at the surfaces, the single-sided sample exhibits less square-like hysteresis loops, as there is less Dy in these area to deter spins flipping. No testing was done to see if there was any remaining Dy on the surfaces, so it cannot be assumed that the Dy coating reserves were exhausted in the samples examined.

Based on the results of the lowDy samples annealed in Mo casing, (Figure 3.6) the single-sided coatings experienced generally less $\boldsymbol{H_{cJ}}$ enhancement. However, there were also reduced $\boldsymbol{B_r}$ loses and hence a higher $(BH)_{max}$ than the double-sided magnets.

4.1.3 Microstructure

It is evident from the SEM images that the Dy is concentrated at areas closer to the magnetic surface, where it substitutes Nd to a greater extent in the harder magnetic phase to form $(Dy, Nd)_2Fe_{14}B$. The BSE and WDX images agree with the established belief that the Dy travels first through the grain boundaries, and is then included in the hard magnetic phase and appear very similar to those presented by Li[52], although the diffusion depths are only about 20 µm due to smaller heat treatment times. In areas where more Dy is incorporated into the magnet, the grain boundary itself is no longer visible as the Dy dispersion appears to be homogeneously dispersed throughout the grain boundaries and the edge of the $(Nd, Dy)_2Fe_{14}B$ grains. This agrees with results obtained by Li[9] and Popov[12]. In areas where Dy is present, particularly the grain boundary, the amount of Nd is generally reduced. This is especially-well seen in the lowDy WDX images (Figure 3.13).

Diffusion into the magnet is limited to about 100 µm for both the lowDy and highDy samples, as witnessed by the WDX concentration mappings in Figure 3.14 and Figure 3.17. The amount of Dy present initially in the magnet did not have a great effect of the diffusion depth of Dy throughout the sample. It did have some effect of the maximum and minimum recorded amounts of Dy and Nd, respectively, reported at the sample edges, although these differences were also minimal. Popov et al. found that after GBD of DyCo powders at HT and LT annealings of 750 °C and 550 °C, respectively, the penetration depth into the magnets was about 2.5 µm and the maximum Dy was also located at the surface, also in the vicinity of 10%. The higher diffusion distance in this case may be because a higher initial Nd-content (32%) was present. Because of the short diffusion distance of the Dy into the bulk magnet, GBD is only suitable for small or thin magnets. The diffusion depth found in this work is much less than values reported by Soderžnik[38] and Oono[18] which reported depths of up to 3 mm and 5 mm, respectively. However, the former underwent annealing cycles of up to 10 hours, and the latter employed Dy-Ni-Al powders as diffusion sources.

The equality in diffusion distance may indicate that the grain boundary microstructure in the highDy and lowDy magnets may be very similar, despite the boundaries being less visible in the former. The reason for reduced visibility may be partially due to the atomic weight of Dy and Nd being relatively close, so contrast between the two pure elements using BSE imaging may be difficult to see.

The rapid increase in $\boldsymbol{H_{cJ}}$ with only slight reductions in $\boldsymbol{B_r}$ is believed to be due to the shell-structure of the magnets; this serves as a high-anisotropy layer, for which higher coercive

fields are needed before reverse nucleation occurs. The refinement of the Nd-phase via the LT annealing serves to decouple the grains and further increase the coercivity. Theoretically speaking, H_{cJ} and B_r would increase and decrease (respectively) monotomically with the substitution of Dy for Nd (this is more generally for sintering conditions). However, because of this shell structure protecting not only the individual grains, but also the bulk magnet because of the diffusion occurring from the surface, the nucleation of reverse domains may be retarded for the bulk of the magnet. Thus, H_{cJ} is able to rise at a more rapid rate that B_r falls (as seen when comparing the H_{cJ} and B_r curves for any of the magnet series). However, in this particular project one must be cautious in interpreting data because of the small diffusion depth. This may be only true for these specific magnets because H_{cJ} is most likely is characteristic only of the area in which Dy was interdiffused, whereas B_r is representative of the bulk. Komuro[40] found that thinner magnets employing GBD and DyF powders as the diffusion source witnessed an increased relative coercivity gains per unit increase in wt% Dy applied using GBD. For instance, magnets with thicknesses of 5 mm, 1 mm, and 0,35 mm thickness experienced relative changes in coercivity of 0,45- 0,58- and 2,70 MA/m/wt%, respectively. Hirota[51] found that after annealing magnets under at 900 °C and 500 °C for one hour each, Dy applied via HRE oxide or fluoride powders was still present at 250 µm. After removing 20 µm from the sample surface, the slight decrease in remanence values were recovered, and after removing 50 µm the coercivities were still the same. Samples in the study ranged from [4 mm x 4 mm x 0,5 mm] to [20 mm x 20 mm x 1-5 mm].

The reason for the refinement of the grains and cracking near the surface of the magnet may be due to the rapid cooling of the magnet, either during the sintering process or annealing. The faster the quenching rate of a structure, the more refined are the grains. The sample surface would represent the area cooled most quickly. Conversely, areas near the center of the magnet would cool more gradually, allowing for grain ripening and coarsening. This may also explain the greater substitution of the Dy into the hard magnetic phase near the sample edges: not only would there be a greater respective volume of the grain boundary phase (a higher differential), but the grains are also smaller so the progressive interdiffusion until the center of the grain is reached occurs in less time. It is possible that as the annealing cycles progressed more defects were introduced, which could have led to progressively smaller grains and hence even more rapid interdiffusion to the grain centers. Another source of microstructural damage may be the adherence of the magnets to the casing, which may be why the damage in the highDy

magnet (with casing) appears slightly worse than the lowDy magnets (in argon, without Mo casing).

The diffusion of Dy along the grain boundary into the magnet may have been hindered by the microstructure of the grain boundaries. In order to have effective diffusion, the boundary should be continuous. SEM images of the highDy magnets were made after the low temperature annealing. These seem to exhibit a greater degree of cracking and porosity near the sample surface of the highDy sample than the lowDy sample. As mentioned in previous sections, Nd has been shown to increase the fracture resistance of NdFeB magnets, so the small increases in Nd for the lowDy sample may be the reason for the smaller amount of apparent damage.

The amount of rare earths present at any given area within the magnet is about 30%. This is evident in Figure 3.14 and Figure 3.17, in which the sum of weight percentages of Dy, Nd and Pr is relatively constant throughout the sample. The stoichiometric nature of the $(Nd, Dy)_2Fe_{14}B$ grains only allows for a distinct amount of rare earths to be incorporated, everything else must be forced to the grain boundary phase or into rare-earth-rich pockets. This may explain the larger areas of Nd-rich phase in the highDy magnet compared to the lowDy magnet (Figure 3.11 and Figure 3.15). From the WDX images, it can be seen that there are no Fe-rich phases. Given this, the likelihood of an α-Fe phase having formed is low. This is good for the system, as α-Fe can be detrimental to $\boldsymbol{H_{cJ}}$.

No images were made of the magnets before annealing began. It would be interesting to investigate reference magnets in order to determine the microstructure before annealing, especially with respect to the form of the grain boundary and microstructure of the grain near the sample edges. Also, by comparing the analyzed magnets to an uncoated sample, the relocation of the light rare-earth elements could be observed, namely if the Nd and Pr leaving the surface was diffused into the center of the magnet or out of the magnet.

4.2 Dy-Cu Coatings

Compared to the pure-Dy coatings, the Mo foil seemed to adhere to a greater extent to the coatings containing Copper. The more ductile nature of Cu over Dy was observed when removing the Mo dividers between magnets, especially in the samples with thicker Cu coatings. From this, it could not be determined whether the Dy-rich eutectic or the Cu-rich eutectic made a difference in the diffusion characteristics of the coatings. Dy-rich eutectic composition coatings may have performed better only because there was very

little Cu in the system; this is true of both coating removal and the resulting magnetic properties of the samples.

Because it has been shown an increase in Dy content also leads to an increase in H_{cJ}, it is likely that the addition of Cu exceeding ~0,023% may have an adverse effect on the magnetic properties. Because the Cu was applied as a coating and allowed to diffuse from the bulk source into the structure, it is reasonable to assume that the Cu concentration near the surface surpasses that within the magnet (in much the same fashion as the distribution of Dy is inhomogeneous). Concentrations of Cu near the surface may exceed optimal amounts and compromise the magnetic properties of the entire system. Previous experiments in which improvements in the coercivity were observed may differ from the current work in that Cu was introduced to the system as a powder during sintering, allowing for a more uniform dispersion throughout the bulk of the magnet. The Cu in these experiments has been said to lead to refinement of the grain structure, which in the case of the current work is already largely determined by the sintering conditions (before annealing, when Cu enters the system). Additionally, the annealing temperatures used in the sources were much lower than 900 °C. By viewing Figure 1.23, it can be seen that Cu-Nd systems may have a reduced melting point of about 520 °C. Considering this, annealing at 900 °C may have been unnecessary or even detrimental. The melting point of a Cu-Dy compound may have also been decreased to about 800 °C, according to the phase diagram presented in Figure 1.23.

Although there was an increase in H_{cJ} when small amounts of Cu were employed, it does not exceed the increases witnessed when only Dy was added to the system. Thus, for the purposes of this experiment, Cu additions were not considered beneficial to the system and SEM analysis was not performed. Unlike the lowDy samples, the addition of Cu in the highDy samples does not have as adverse of an effect on the coercivity. This is probably due to the higher amount of Dy present, which would counter-act H_{cJ} losses due to Cu to some extent.

Although the values of H_{cJ} with small additions of Cu were comparable to those with only Dy, the reduction of B_r with Cu inclusion rules out Cu as a beneficial element within the scope of this work.

Chapter 5 - Conclusions

The purpose of this work was to increase H_{cJ} of NdFeB permanent magnets without substantial reductions in B_r. This was done through the process of grain-boundary diffusion (GBD), in which coatings were applied to magnetic samples by PVD and allowed to interdiffuse into the magnet during annealing. Two kind of magnets were used: one variation containing 0,5 wt% Dy initially, and one containing 4,5 wt% Dy initially. These were then coated using PVD with various thicknesses of Dy and Dy-Cu coatings, which were then allowed to interdiffuse into the magnet during an annealing process at 900 °C. The high temperature annealing was followed by a low-temperature annealing at 500 °C for 1 hour, after which the magnetic properties were measures. This process was repeated until a plateau in the coercivity was reached.

It was found that small additions of Dy, up to about 1,24 % for samples containing lower amounts of Dy and 4,86% for samples with higher initial amounts of Dy, were able to be included without significantly decreasing the remanence. This may be because the reported H_{cJ} is indicative of areas near the surface where Dy inclusion is a maximum (~10 wt%), whereas B_r is representative of the entire sample. This aspect must be considered before applying the results of this work to other projects using samples with different dimensions. A more thorough investigation into the magnetic properties of areas near the surface of the samples will be left as potential for future research. It was also observed that the samples containing the same amount of Dy, but with the coating only applied on one side, had lower reductions in B_r and lower increases in H_{cJ}, compared to those with coatings applied on both sides. Samples with single-sided coatings also displayed less square-like hysteresis loops indicating that the structure is less homogeneous. This is reinforced by WDX concentration profiles, in which the depth of Dy interdiffusion was found to be about 100 µm for both kinds of magnets. The BSE images also display inhomogeneous distributions of Dy, with a higher level of Dy substitution in the hard magnetic grain closer to the magnet surface.

The inclusion of Cu was, in the frame of this work, found to be general disruptive to the magnetic properties of the sample, both in regards to H_{cJ} and B_r. In small amounts, gains in coercivity were still able to be made in comparison to an uncoated, non-annealed sample; however, this is thought to be because of the conclusion of Dy in the structure. The reason for these results may be the addition of Cu at a coating, which allows for over-optimal amounts of Cu to be concentrated in areas of the magnet in which it was diffused.

References

[1] Gignoux, D., Schlenker, M. *Magnetism: Materials and Applications*. First Springer Science+Business Media Inc: New York, NY. 2005

[2] K.H.J. Buschow, F.R. de Boer. *Physics of Magnetism and Magnetic Materials.* Kluwer Academic Publishers: New York. 2003. 3-9

[3] J. Stöhr, H.C. Siegmann. *Magnetism: From Fundamentals to Nanoscale Dynamics.* Springer-Verlag: Berlin Heidelberg. 2006.

[4] Dr. Vitor Amaral. Lecture Slides: *Physical Properties of Materials*. Universidade de Aveiro, Portugal. September. 2011.

[5] W. Martienssen, H. Warlimont. *Springer Handbook of Condensed Matter and Materials Data*. Springer: Berlin Heidelberg 2005

[6] Alloul, Henry. *Introduction to the Physics of Electrons in Solids.* Springer: Berlin Heidelberg. 2011. 283-284

[7] J. Coey. 5006 Magnetism and Magnetic Materials Lecture Notes. Trinity College, Dublin. March 2007.

[8] Liu Y, Sellmyer D, Shindo D. *Handbook of Advanced Magnetic Materials:Volume I:Advanced Magnetic Materials: Nanostructural Effects*. Springer Science Business + Media, Inc: New York, NY. 2006

[9] W.F. Li, H. Sepehri-Amin, T. Ohkubo, N. Hase, K. Hono. Acta Materialia **59** (2011) 3061–3069.

[10] H. Sepehri-Amin, T. Ohkubo, K. Hono. J. Appl. Phys. **107**, 09A745 (2010).

[11] H. Nakamura, K. Hirota, M Shimao, T. Minowa, M. Honshima. IEEE Transactions on Magnetics **41**. No. 10, (2005).

[12] Popov, Yasilenko, Puzanova, Shitov, Vlasyuga. The Physics of Metals and Metallography **111**(5), (2011) 471–478.

[13] H. Suzuki, Y. Satsu, M. Komuro. J. Appl. Phys. **105**, 07A734 (2009)

[14] Dr. Bernd Stritzker. Lecture slides: *Materials Physics*. October 2010

[15] Mehrer, Helmut. *Diffusion in Solids*. Springer Verlag: Berlin Heidelberg. 2007.

[16] W. Sprengel, S. Herth, V. Barbe, H-E Schaefer, T. Wejrzanowski. Journal of Applied Physics **98**, 074314 (2005)

[17] Vacuumschmelze GmbH & Co. KG. *Rare Earth Permanent Magnets: VACODYM, VACOMAX.*

[18] Oono, Sagawa, Kasada, Matsui, Kimura. Journal of Magnetism and Magnetic Materials **323** (2011) 297–300.

[19] W. Li, A.H. Li, H.J. Wang, W. Pan, H.W. Chang. Journal of Applied Physics **105**. (2009)

[20] J.F. Herbst, J.J. Croat, W.B. Yelon. J. Appl. Phys. **57** (1985)

[21] Siemens Internal Use. Grundlagen moderner Dauermagnetwerkstoffe

[22] TechJournal. *HAL Production Process.* (2011).

[23] Lemonick, Michael. *Magnequench Emerges*. Science Digest (1985) 18.

[24] Sugimoto. Journal of Applied Physics **44** (2011).

[25] F. Vial, F. Joly, E. Nevalainen, M. Sagawa, K. Hiraga, K.T.Park. Journal of Magnetism and Magnetic Materials **242–245** (2002) 1329–1334.

[26] G.H. Yan, R.J. Chen, Y. Ding, S. Guo. D. Lee, A.R. Yan. Journal of Physics: Conference Series **266** (2011).

[27] H.D. Nguyen, H.Y. Nguyen, T.T. Pham, T.T.H. Nguyen, H.D Nguyen, et al. Adv. Nat. Sci.: Nanosci. Nanotechnol. **3** (2012).

[28] S. Hirosawa, K. Tokuhara, and M. Sagawa, Jpn. J. Appl. Phys. **26**, L1359 (1987).

[29] Schrefl T, Schmidts HF, Fidler J, Kronmüller H. J Appl Phys. **73** (1993) 6510.

[30] Crew DC, McCormick PG, Street R. Appl Phys Lett **74** (1999) 591.

[31] Sagawa, Masato. REPM '10- Proceedings of the 21st Workshop on Rare-Earth Permanent Magnets and their Applications. (2010).

[32] L. Shandong, B.X. Gu, Y. Sen, B. Hong, D. Yaodong, T. Zongjun, X. Guozhi, D. Youwei, Y. Zuanru. J. Phys. D: Appl. Phys. **35** (2002) 732–737.

[33] T. Fukagawa, T. Ohkubo, S. Hirosawa, K. Hono, J. Magn. Magn. Mater. **322** (2010). 3346.

[34] G. Yan, P.J. McGuiness, J.P.G Farr, I.R Harris. Journal of Alloys and Compounds **491** (2010) L20-L24.

[35] J. F. Herbst, Rev. Mod. Phys. **63**, (1991) 819.

[36] Machida, Suzuki, Kawasaki, Kitamori, Nakamura, Shimizu. Center for Adv. Sci. & Innovation, Osaka Univ., Japan. Magnetics Conference, 2005. INTERMAG Asia 2005. Digests of the IEEE International, (2005) 947-948.

[37] F. Xu, J. Wang, X. Dong, L. Zhang, J. Wu. Journal of Alloys and Compounds **509** (2011) 7909–7914.

[38] M. Soderžnik, K. Rožman, S. Kobe, P. McGuiness. Intermetallics **23** (2012) 158-162.

[39] K. Hirota, T. Ohashi, H. Nakamura, T. Minowa, M. Honshima. *Proceedings of 20th international workshop on rare earth permanent magnet & their applications.* (2008) 122.

[40] M. Komuro, Y. Satsu, H. Suzuki. IEEE Transactions on Magnetics, **46**(11). (2010)

[41] *Binary Alloy Phase Diagrams*, Ed. by T. B. Massalski, 2nd ed. (ASM International, Materials Park, OH, 1996).

[42] J. Fidler and T. Schrefl, *Overview of Nd–Fe–B Magnets and Coercivity*, J. Appl. Phys. **79**, (1996) 5029–5034.

[43] K. T. Park, K. Hiraga, and M. Sagawa, Proceedings of the 16th Workshop Rare-Earth Magnets and Their Applications, Sendai, 2000 (unpublished), 257–264.

[44] D. Li, S. Suzuki, T. Kawasaki, and K. Machida, Jpn. J. Appl. Phys. **47**, 7876 (2008).

[45] N. Watanabe, M. Itakura, N. Kuwano, D. Li, S. Suzuki, and K. Machida, Mater. Trans. **48**, (2007) 915.

[46] GPDP from Neomax

[47] Y. Shinba, T.J. Konno, K. Ishikawa, K. Hiraga. Journal of Applied Physics **97** (2005).

[48] Gabay, Marinescu, L, Liu, Hadjipanayis. J. Appl. Phys. **109,** 083916 (2011).

[49] M. Velicescu, W. Fernengel, W. Rodewald, P. Schrey, B. Wall. Journal of Magnetism and Materials **157/158** (1996) 47.

[50] A.S. Kim, F.E. Camp. IEEE Transations on Magnetics, **31**(6) (1995) 3620-3622.

[51] K. Hirota, H. Nakamura, T. Minowa, M. Honshima. IEEE Transactions on Magnetics, **42**(10), (2006).

[52] D.S. Li, M. Nishimoto, K. Nishiyama, M. Itoh, K. Machida. IOP Conf. Series Materials Science and Engineering **1** (2009) 012020.

[53] http://www.uni-muenster.de/Mineralogie/en/ausstattung/mikrosonde.html. Accessed: Aug, 2012

[54] R S Mottram, A J Williams and I R Harris. *J. Magn. Magn. Mater.* **217**. (2007) 27-34

[55] S. Pandian, V. Chandrasekaran, G. Markandeyulu, K.J.L Iyer, K.V.S Rama Rao. J. Appl. Phys. **92**, (2002) 6082.

[56] C.D. Fuerst, E.G. Brewer. Appl. Phys. Lett. **56**, (1990) 2252.

[57] O.M. Ragg, I.R. Harris. Journal of Alloys and Compunds **256**. (1997) 252-257.

[58] G. Bai, R.W. Gao, Y. Sun, G.B. Han, B. Wang. **308**. (2007) 20-23.

[59] S. Szymura. Journal of Less-Common Metals **175**. (1991) 185-198.

[60] Cardarelli, François. *Materials Handbook: A Concise Desktop Reference, 2nd Edition*. Springer Verlag: London. 2008. 487-517

[61] J. Fidler. *Proc. 7th Int. Symp. On Magnetic Anisotropy and Coercivity in Rare-Earth Transition Metal Alloys, Canberra, Austrailia 1992. p. 11*

Appendix A : Alloying Materials and Effects

Appendix A : Alloying Materials and Effects

Group	Element	Purpose	Decreases	MP [°C]	Density [kg/m^3]	Atomic mass [g/mol]	% Optimal	Source
Group IB	**Cu**	Increases $\boldsymbol{H_c}$, working temperature, and the energy density and corrosion resistance by enriching/replacing the Nd-rich phase with ReCu (which has a reduced MP) and encompassing the magnetic grains. This leads to a refined microstructure which impedes the growth of RDs. The formation of an $Re_6Fe_{13}Cu$ phase in magnets with low Boron content has also been reported[49]. **(M_1)**	$\boldsymbol{B_r}$, T_c[55]	1084	8960	63,546	0,15%	[50]in conjunction with Co
							0,5 wt%	[56]
							0,3 at%	[49]with Co and Dy ($Nd_{13}Dy_1Co_{3,3}Cu_{0,3}B_6Fe_{bal}$)
							0,25 at%	[57]after 150 min at 500 °C
Group IIB	**Zn**	Encompasses the magnetic grain, impeding the growth of RDs, diffuses thoroughly through NdFeB magnets[56]. **(M_1)**		420	7133	65,409	0,8 wt%	[56]
Group IIIA*	**B**			2075	2340	10,811		
	Al	Increases $\boldsymbol{H_c}$ by decreasing the MP of the Nd-rich phase, to increase wetting of the magnetic grains and deter RD growth. Enters the matrix phase to increase the c/a ratio. Enters both the matrix and GB phase, forming a paramagnetic Nd(Fe, Al) phase at the grain interfaces, but reducing the amount of matrix phase. **(M_1)**	$\boldsymbol{B_r}$, $(BH)_{max}$, T_c (~8 K/at%)	660	2698,9	26,982	< 1wt%	[55]based on composition data
							2 at%	[54]after heat treatment
							1,5 at%	[54]in conjunction with Co
	Ga	Increases $\boldsymbol{H_c}$, corrosion and thermal stability by enriching the GB encompassing the magnetic grain, increasing XL anisotropy and inducing texture, which impedes the growth of RD. The Ga which enters the hard grains substitutes for Fe, which because Ga is non-magnetic, enhances uniaxial anisotropy. **(M_1)**	$\boldsymbol{B_r}$, B_s, $(BH)_{max}$	30	5907	69,723	1-3 wt%	[55]based on composition data
	In	Surrounds magnetic grain to impede the growth of RD.		156	7310	114,818		
Group IVA	**C**	Substitutes B.		n/a	2260	12,01		
	Sn	Increases $\boldsymbol{H_c}$. **(M_1)**	$\boldsymbol{B_r}$, $(BH)_{max}$	232	7298	118,711		

Group	Element	Purpose	Decreases	MP [°C]	Density [kg/m^3]	Atomic mass [g/mol]	% Optimal	Source
Group IVB	**Ti**	Decreases the MP of the Nd-phase. T_c = 663 K. **(M_2)**	Vickers Hardness	1668	4540	47,867		
	Zr	Refines the grain structure. **(M_2)**		1855	6506	91,224		
Group VB	**V**	Increases corrosion and temperature stability by refining the grain structure. **(M_2)**	B_r, $(BH)_{max}$	1890	6160	50,941	1,5 wt%	[58]used in $Nd_{27}Dy_4Fe_{(bal)}Co_2Ga_xB$
	Nb	Increases corrosion and temperature stability by refining the grain structure. **(M_2)**	B_r, $(BH)_{max}$	2468	8570	92,906	0,4wt%	[55]based on composition data
Group VIB	**Cr**	Increases H_c.	B_r, $(BH)_{max}$	1857	7190	51,996		
	Mo	Increases H_c and leads to a refined grain structure. **(M_2)**	B_r, $(BH)_{max}$	2622	10220	95,94		
Group VIIIB	**Mn**	Substitutes Fe, only diffuses over short distances[56].		1244	7440	54,938		
Group VIII(1)	**Fe**	T_c = 1043 K.		1534	7874	55,845		
Group VIII(2)	**Co**	Increases M_s, T_c, thermal stability and corrosion resistance by refining the microstructure. Substitutes F, decreasing H_c due to planar anisotropy of Co[59]. Replaces the Nd-rich phases with Re_3Co (which has a MP). T_c = 1394 K.	H_c	1455	8900	58,933	1,20%	[50]in conjunction with Cu
							5 at%	[54]
							5 at%	[54]in conjunction with Al
							3-5 at%	[49]
							3,3 at%	[49]with Cu and Dy
Group VIII(3)	**Ni**	Decreases the MP of the Nd-phase. T_c = 663K.		1452	8902	58,693		
Lanthanide	**Nd**			1021	7007	144,24		
	Tb	Increases H_c by substituting for Nd.	B_r, $(BH)_{max}$	1356	8229	158,925		
	Dy	Increases H_c, working temperature, improves impact stability.	B_r, $(BH)_{max}$	1412	8551	162,5	1 at %	[49]with Co and Cu

*MP = Melting Point, XL = Crystalline, GB = Grain Boundary, RD = Reverse Domains
**MP, Density, Atomic mass values taken from [60]
M_1 – forms Nd-M_1 of Nd-Fe-M1 intergranular or intragranular phases[60]
M_2 – forms M_2B or Fe-M_2-B intergranular or intragranular phases[60]